

Initial conditions for star formation in clusters: physical and kinematical structure of the starless core OphA-N6

Tyler L. Bourke¹, Philip C. Myers¹, Paola Caselli², James Di Francesco³, Arnaud Belloche⁴, René Plume⁵, David J. Wilner¹

ABSTRACT

We present high spatial (<300 AU) and spectral (0.07 km s^{-1}) resolution Submillimeter Array observations of the dense starless cluster core Oph A N6, in the 1 mm dust continuum and the 3-2 line of N_2H^+ and N_2D^+ . The dust continuum observations reveal a compact source not seen in single-dish observations, of size ~ 1000 AU and mass $0.005\text{-}0.01 M_\odot$. The combined line and single-dish observations reveal a core of size 3000×1400 AU elongated in a NW-SE direction, with almost no variation in either line width or line center velocity across the map, and very small non-thermal motions. The deuterium fraction has a peak value of ~ 0.15 and is > 0.05 over much of the core. The N_2H^+ column density profile across the major axis of Oph A-N6 is well represented by an isothermal cylinder, with temperature 20 K, peak density $7.1 \times 10^6 \text{ cm}^{-3}$, and N_2H^+ abundance 2.7×10^{-10} . The mass of Oph A-N6 is estimated to be $0.29 M_\odot$, compared to a value of $0.18 M_\odot$ from the isothermal cylinder analysis, and $0.63 M_\odot$ for the critical mass for fragmentation of an isothermal cylinder. Compared to isolated low-mass cores, Oph A-N6 shows similar narrow line widths and small velocity variation, with a deuterium fraction similar to “evolved” dense cores. It is significantly smaller than isolated cores, with larger peak column and volume density. The available evidence suggests Oph A-N6 has formed through the fragmentation of the Oph A filament and is the precursor to a low-mass star. The dust continuum emission suggests it may already have begun to form a star.

Subject headings: ISM: individual (Oph-A N6) – stars: formation – stars: low-mass

¹Harvard-Smithsonian Center for Astrophysics, 60 Garden Street, Cambridge, MA 02138; email tbourke@cfa.harvard.edu

²School of Physics & Astronomy, E.C. Stoner Building, The University of Leeds, Leeds, LS2 9JT, UK

³National Research Council Canada, Herzberg Institute of Astrophysics, Victoria, BC, Canada

⁵Max-Planck-Institut für Radioastronomie, Auf dem Hügel 69, D-53121 Bonn, Germany

⁴Department of Physics and Astronomy, University of Calgary, Calgary, AB, Canada

1. Introduction

It is now well established that low-mass (i.e., solar-like) stars form from the collapse of dense cores within molecular clouds (e.g., Larson 2003). The initial conditions of isolated star formation are known from continuum and line observations of many tens of dense cores in molecular cloud complexes such as Taurus, with relatively sparse concentrations of young stars (Di Francesco et al. 2007). The best commonly observed molecular line tracers of the central few thousand AU of centrally condensed cores on the verge of star formation are NH_3 (ammonia), N_2H^+ , and N_2D^+ (Caselli et al. 2002c; Tafalla et al. 2002; Crapsi et al. 2005, 2007). Observations of these lines and the dust continuum have enabled the properties of dense isolated starless cores thought to be near to or at the point of star formation to be well determined in recent years (Di Francesco et al. 2007; Bergin & Tafalla 2007). These properties include (i) a high degree of deuterium fractionation, (i.e., large $\text{N}(\text{N}_2\text{D}^+)/\text{N}(\text{N}_2\text{H}^+)$) (ii) a large central density ($\sim 10^6 \text{ cm}^{-3}$), (iii) depletion of CO and other C-bearing species, (iv) cold central regions ($< 10 \text{ K}$), and (v) line asymmetries indicative of infall motions.

In this paper, we present the first detailed observational study of the internal structure of a starless cluster core, to explore how star formation in clusters compares to isolated star formation. Most stars are believed to form in close proximity to other stars within embedded clusters (Lada & Lada 2003; Allen et al. 2007; Bressert et al. 2010). As a result, a fundamental problem in astrophysics is whether star formation in cluster environments is similar to better-understood isolated star formation, or whether cluster star formation is more turbulent and dynamic. An important question is to what degree do stars in clusters form in the same way as in isolation, i.e., from cores whose properties strongly influence the stellar properties (Shu et al. 2004; Larson 2005; Tan et al. 2006; see reviews by Shu et al. 1987; Larson 2003), and to what degree do they form in a different, more dynamic way, where external forces and interactions matter more than initial conditions (e.g., Bonnell et al. 2001; Bonnell & Bate 2006).

A number of observational studies made over recent years have provided information on the global properties of dense cores within nearby cluster-forming regions (Ward-Thompson et al. 2007). Dust continuum observations tracing high column densities have been more numerous, due to their faster mapping speeds compared to molecular line observations. As a result, large maps have been made of molecular clouds containing embedded clusters in Ophiuchus (L1688; Motte et al. 1998; Johnstone et al. 2000; Stanke et al. 2006; Young et al. 2006), Perseus (NGC 1333, IC348-SW; Sandell & Knee 2001; Hatchell et al. 2005; Enoch et al. 2006; H. Kirk et al. 2006), Corona Australis (Chini et al. 2003; Nutter et al. 2005), Serpens (Davis et al. 1999; Enoch et al. 2007), and the more distant and massive Orion cluster (Chini

et al. 1997; Lis et al. 1998; Johnstone & Bally 1999; Li et al. 2007). Some progress has been made in large area mapping of molecular line dense gas tracers with resolution approaching that of dust continuum observations of $\leq 30''$, in nearby low-mass regions (Williams & Myers 2000; André et al. 2007; Walsh et al. 2007; Friesen et al. 2009, 2010a,b), and Orion (Ikeda et al. 2007, 2009; Tatematsu et al. 2008). Although some studies have been able to “resolve” starless cores in clusters in molecular spectral lines (Williams & Myers 2000; Walsh et al. 2007), in the sense that the measured core size is larger than the beam, no study has examined the internal structure of any cluster core in detail. Observations of cores in cluster-forming regions that resolve individual cores are thus needed to understand how these regions can make stars so much more efficiently than in isolation. Progress toward this goal has been slower than for isolated regions. Most young clusters are more crowded so their cores suffer more confusion; their cores are smaller and more distant so they are harder to resolve, and they form stars more frequently so that starless cores are less common (Jijina et al. 1999).

1.1. Ophiuchus A N6

The Ophiuchus molecular cloud, at a distance of only 125 pc (de Geus et al. 1989; Knude & Hog 1998; Loinard et al. 2008; Lombardi et al. 2008), is the nearest example of cluster formation embedded within dense gas and dust, and is an ideal region in which to study the initial conditions for cluster formation (see review by Wilking, Gagné and Allen 2008; Motte et al. 1998; Johnstone et al. 2000, 2004; André et al. 2007; Enoch et al. 2008; Jørgensen et al. 2008; Simpson et al. 2008; Padgett et al. 2008; Friesen et al. 2009, 2010a,b; van Kempen et al. 2009; Gutermuth et al. 2009; Maruta et al. 2010). Within Ophiuchus, the Oph A ridge is the brightest of the clumps in both dust emission and N_2H^+ 1-0, containing 8 dust cores identified through 1.3 mm continuum emission (Motte et al. 1998) and 6 local maxima of integrated N_2H^+ 1-0 emission (Di Francesco et al. 2004, hereafter DAM04; André et al. 2007). The N_2H^+ cores in the main part of the ridge, where the dust emission is strongest, show line widths that are not significantly different from those observed toward isolated starless cores (Di Francesco et al. 2004; Crapsi et al. 2005). In this region, N6 is the best core for studies of internal structure as it is isolated from the other Oph A cores (thereby suffering less from confusion), is bright in molecular lines, and is larger and thus better resolved than the other Oph A cores (Di Francesco et al. 2004; Pon et al. 2009). For these reasons, we have undertaken high angular resolution submillimeter observations of N6 using the Submillimeter Array in the high density gas tracers N_2H^+ and N_2D^+ 3-2, and combined those data with single dish observations using the James Clerk Maxwell Telescope (JCMT) and Institut de Radioastronomie Millimétrique (IRAM) 30-m telescope.

This paper is divided into the following sections. In §2 we present our observations using the Submillimeter Array (SMA), JCMT, and IRAM 30-m, in §3 we present the line and continuum results, §4 presents the analysis, including the column densities, deuterium fraction, and structure of N6, §5 presents a discussion on the structure and evolution of N6, and compares it to both isolated cores and cores within cluster-forming regions, while a summary is presented in §6.

2. Observations

2.1. Submillimeter Array

Observations in the N_2D^+ 3-2 line toward Oph A-N6 were undertaken with the SMA on 2006 July 22. The array was in its compact configuration and zenith opacities at 225 GHz were typically 0.1-0.13. The SMA correlator was configured with 2048 channels over 104 MHz for the N_2D^+ 3-2 line at 231.321 GHz, providing a channel spacing of 0.066 km s^{-1} . This high resolution mode decreases the available bandwidth for continuum observations, resulting in 1 GHz of continuum bandwidth in the upper sideband and 1.15 GHz in the lower. The effective continuum frequency is 226 GHz (1.3 mm). The observations of Oph A N6 were interleaved with the quasar J1626-298 for complex gain calibration. Uranus and 3c454.3 were used for bandpass calibration, and Uranus was also used for flux calibration. The data were calibrated and edited in the SMA’s MIR software package.

Observations in the N_2H^+ 3-2 line toward Oph A-N6 were undertaken with the SMA on 2007 March 30. The array was in its compact configuration and zenith opacities at 225 GHz were typically ~ 0.06 . The SMA correlator was configured with 2048 channels over 104 MHz for the N_2H^+ 3-2 line at 279.512 GHz, providing a channel spacing of 0.055 km s^{-1} . This high resolution mode decreases the available bandwidth for continuum observations, resulting in 1.3 GHz of continuum bandwidth in both the upper and lower sidebands. The effective continuum frequency is 276 GHz (1.1 mm). The observations of Oph A-N6 were interleaved with the quasars J1626-298 and J1517-243 for complex gain calibration. The quasar 3c279 was used for bandpass calibration, and Titan and 3c279 were used for flux calibration. The data were calibrated and edited in the SMA’s MIR software package.

Further observations in the N_2H^+ 3-2 line toward Oph A-N6 were undertaken with the SMA on 2007 May 2, with the array in its subcompact configuration. Zenith opacities at 225 GHz were typically 0.06-0.08. The correlator setup, resolution, available continuum bandwidth, and complex gain calibrators were the same as for the 2007 March 30 observations. Neptune and 3c273 were used for bandpass calibration, and Neptune was also used for flux

calibration. The data were calibrated and edited in the SMA’s MIR software package.

Based upon independent observations of the gain and passband quasars at similar frequencies (± 10 GHz) and times (within one month), and upon independent calibration of the observations presented here, as part of the SMA’s ongoing monitoring of quasar fluxes¹, we estimate the flux calibration to be good to 20% for all our observations.

2.2. JCMT

Observations in the N_2D^+ 3-2 line toward Oph A-N6 were undertaken with the James Clerk Maxwell Telescope (JCMT) between February and July 2005. All observations were made on a 5×5 grid with $10''$ spacing, with angular resolution of $22''$, and a spectral resolution of 0.1 km s^{-1} . Details of the observations have been presented in Pon et al. (2009), and the reader is referred to that paper for further information.

2.3. IRAM 30-m

Observations of Oph A-N6 with the IRAM 30-m telescope were undertaken in May 2007 as part of a larger mapping program of the Oph A ridge. Although four SIS heterodyne receivers were used simultaneously in the 3, 2, and 1.2 mm atmospheric windows, here we only focus on the observations of N_2H^+ 3-2 at 279.511 GHz that are used in this paper. The autocorrelation spectrometer VESPA was used as backend with a channel spacings of 40 kHz and bandwidth of 80 MHz. The system temperature ranged from 650 to 3620 K and the pointing was checked every 1–2 hours on bright quasars and found to be good to 2–3'' (rms). The telescope focus was optimized on Saturn and Jupiter every 3–4 hours. At the frequency of N_2H^+ 3-2 the telescope beam size (full-width at half-power) is $9''$. The observations were performed in position-switching mode with the OFF position offset by $(\Delta\alpha, \Delta\delta) = (-900'', 0'')$ from the nominal map center of $16^{\text{h}}26^{\text{m}}26^{\text{s}}.46$, $-24^{\circ}24'30.8''$, located at VLA 1623. No emission was found at the OFF position down to an rms noise level of 0.42 K in T_a^* scale. Mapping was done in on-the-fly scanning mode with a step of $4''$, providing fully sampled maps. We scanned alternately in right ascension and declination to avoid striping artefacts. The data were reduced using the CLASS software in its Fortran 90 version²

¹see <http://sma1.sma.hawaii.edu/callist/callist.html>

²see <http://www.iram.fr/IRAMFR/GILDAS>

2.4. Combined Interferometric and Single-Dish Observations

The procedure used to combine the interferometric and single dish data sets is similar to that described by Zhang et al. (2000) and Takakuwa et al. (2007), and is based on the methods described in Vogel et al. (1984) and Wilner & Welch (1994). The MIRIAD software package (Sault et al. 1995) was used for the combination and subsequent imaging.

2.4.1. N_2D^+ 3-2: SMA + JCMT

For the N_2D^+ 3-2 observations, the data sets were resampled along the velocity axis to a channel spacing of 0.07 km s^{-1} . The JCMT data were converted to Jy using a conversion factor of $S(\text{Jy}) = 27.4 \times T_A^*(K)$, and deconvolved with a $22''$ FWHM Gaussian used to represent the JCMT beam at 231 GHz. Next, the JCMT data were convolved by a $55''$ Gaussian representing the SMA primary beam (full width at half power). Side lobe effects are not well known and are thus ignored. Then the JCMT image cube was fourier transformed into a visibility data set, with a sampling density in the (u,v) plane chosen to closely match that of the SMA in their overlap region. Finally, the JCMT and SMA visibility data sets were fourier transformed together back into the image plane. Because of the extended nature of the emission, a correction for the SMA primary beam attenuation away from the phase center was applied. With a robust weighting of 0 applied during the transform, the resultant image cube has a resolution of $5''.1 \times 3''.4$ (synthesised beam full-width at half power) with a 1σ rms sensitivity of $0.43 \text{ Jy beam}^{-1} \text{ channel}^{-1}$.

2.4.2. N_2H^+ 3-2: SMA + 30-m

The procedure for combining the SMA and 30-m N_2H^+ 3-2 data sets is the same as that used for the SMA and JCMT data sets. The data sets were first resampled along the velocity axis to a channel spacing of 0.07 km s^{-1} , for direct comparison with the N_2D^+ 3-2 data. A conversion factor of $S(\text{Jy}) = 9.3 \times T_A^*(K)$ was used for the 30-m data, and the assumed Gaussian beams sizes used were $8''.8$ and $45''$ for the 30-m and SMA respectively at 279.5 GHz. The 30-m and SMA visibility data sets were fourier transformed together using a robust weighting of 0 with a Gaussian taper of $2''$. Because of the extended nature of the emission, a correction for the SMA primary beam attenuation away from the phase center was applied. The resultant image cube has a resolution of $5''.6 \times 3''.7$, similar to that of the N_2D^+ 3-2 cube, with a 1σ rms sensitivity of $0.72 \text{ Jy beam}^{-1} \text{ channel}^{-1}$. A comparison of the central spectra of the combined SMA + 30-m dataset with the 30-m only dataset, after

smoothing the SMA + 30-m dataset to the angular resolution of the 30-m dataset, shows that essentially all of the single-dish flux is recovered, and the line-shapes are very similar.

2.5. Continuum imaging

The MIRIAD software package was used to fourier transform and produce images from the interferometric-only continuum data. At 226 GHz (1.3 mm) a robust weighting of 2 was used with a 3'' taper, to improve the sensitivity, resulting in a resolution of 5''.2 × 4''.3 with a 1σ rms sensitivity of 2.6 mJy beam⁻¹. At 276 GHz (1.1 mm) a robust weighting of 0 was used with a 3'' taper (note that with both compact and subcompact array data, a robust weighting of 2 would excessively down-weight the longer baselines), resulting in a resolution of 4''.6 × 3''.5 with a 1σ rms sensitivity of 3.6 mJy beam⁻¹.

3. Results

3.1. Molecular line maps

Figure 1 shows the integrated line maps of N₂D⁺ 3-2 and N₂H⁺ 3-2, compared to the distribution of integrated N₂H⁺ 1-0 emission within the entire Oph A ridge (DAM04). The integration is performed over the hyperfine structure, corresponding to velocity ranges of 3.23–4.56 km s⁻¹ (N₂D⁺) and 0.22–6.18 km s⁻¹ (N₂H⁺). The general agreement between the N₂D⁺ and N₂H⁺ emission is good, but their peaks are offset by 9'' (Figure 2). Similarly, the N₂H⁺ 1-0 map has its peak offset from the N₂D⁺ 3-2 map, and shows good positional coincidence with N₂H⁺ 3-2. The offsets between N₂H⁺ and N₂D⁺ could be due to optical depth effects (see §4.1), or chemical differentiation (Pon et al. 2009). Figure 2 also shows that the 3-2 maps have slightly different position angles. The N₂D⁺ 3-2 map is closely aligned with the N₂H⁺ 1-0 map, although their peaks do not coincide.

The N₂H⁺ 3-2 spectrum is composed of three groups of hyperfine (hf) features. Integrated maps of these hyperfine groups are shown in Figure 3, labelled according to their velocity offsets relative to the line frequency as “low-V”, “main-V”, and “high-V”. The low-V and high-V groups are sometimes referred to as the satellite hyperfine groups. Figure 3(a) shows the spectrum at the position of peak integrated emission in the main-V map, with the positions and relative intensities of the hyperfine components in the optically thin case indicated. The main-V group shows considerable saturation for the components in the range 3.5–4.0 km s⁻¹, indicating large optical depths (confirmed through fitting of the hyperfine structure, see §4.1). As a result, the integrated map of the main-V group is larger than that

of the other hyperfine groups and the region of peak emission is more extended. The peaks of the satellite hyperfine groups, low-V and high-V, are not coincident, as might be expected as they both account for the same relative line strength. Instead, the high-V group peaks at the same position as the main-V group, while the low-V group peaks at the position of peak N_2H^+ 1-0 emission (DAM04). The reason for this is not clear; perhaps it suggests that non-LTE excitation anomalies, as seen in the 1-0 line (Caselli, Myers & Thaddeus 1995; Daniel, Cernicharo, & Dubernet 2006) are present in the 3-2 line. Modelling of the current observations with a non-LTE line code that does not assume the hyperfines are in statistical equilibrium (Keto & Caselli 2010) could potentially address this question, but is beyond the scope of this paper. The satellite hyperfines are particularly strong in N6, both in absolute intensity, and in their relative intensity compared to the main-V group. Their relative strength compared to the main-V group is mostly due to the high total optical depth, as noted. However, their absolute intensity is about an order-of-magnitude brighter than has been seen toward any other low-mass starless core, for example by comparison to L1544, using just the 30-m data for each core (Caselli et al. 2002a,b; Daniel et al. 2007).

The map sizes as traced by the molecular line emission have been estimated through two dimensional Gaussian fitting to the integrated maps, and through approximate measurements by eye using the contour level tracing 50% of the peak emission in the same maps. The results are similar for both methods for each line, suggesting the integrated emission can be approximated by a Gaussian. For N_2H^+ 3-2, we only used the maps of the low-V and high-V emission to estimate the size, so including N_2D^+ we used three maps in all. All maps and methods give consistent results, with the half-maximum diameter measured to be $\sim 3100 \times 1600$ AU, with uncertainties of a few hundred AU for each axis. The geometric mean diameter is ~ 2200 AU, which is smaller than the geometric mean diameter of ~ 3400 AU determined by DAM04 through N_2H^+ 1-0 observations, likely due to the finer resolution of the observations presented here ($5''$ cf. $10''$). The ratio of major-to-minor axes is about 2:1. The core is well-resolved, as each axis is significantly greater than the beam diameter (640×425 AU for N_2D^+ , 700×460 AU for N_2H^+).

3.2. Dust continuum emission

Weak dust continuum emission is detected at both 1.3 mm and 1.1 mm (Fig. 4). Unlike the emission in the single-dish map (Fig. 4a; Motte et al. 1998), N6 is a local peak of emission at these frequencies. The interferometer has effectively filtered out the larger scale bright emission to reveal the weak emission associated with N6. More extended emission is missing from the 1.3 mm map due to the array configurations used, and this may be enough to

cause the emission in this map to look smaller than the 1.1 mm emission. The dust emission is similar in size and orientation at both wavelengths, with a small offset ($3''.5$) between their peaks. However, this offset is at the 1σ flux level and so is probably not significant. The orientation of the dust emission is very similar to that of the molecular line emission (Figure 5), and to that of the large scale dust emission.

The mass of the region traced by the dust emission can be determined in the standard manner (Hildebrand 1983) using the flux density of the region. For these calculations we use the peak dust temperature of 20 K (Pon et al. 2009), a gas-to-dust ratio of 100, and assume the dust opacity is given by the commonly used “OH5” opacities that are believed to best represent the dust properties within cold dense regions (Ossenkopf & Henning 1994; Evans et al. 2001). Using the flux density above the 2 sigma level leads to a total mass estimate of $0.011 M_{\odot}$ at both 1.3 mm and 1.1 mm. Using the 3 sigma level as the cutoff, the mass estimates are $0.006 M_{\odot}$ at 1.3 mm and $0.005 M_{\odot}$ at 1.1 mm. Thus the values at 1.3 mm and 1.1 mm are in agreement. At the 3 sigma intensity level the core size is of order 1000 AU at both wavelengths, much smaller than the size of the line emitting regions. This small size may be due to large scale structure being resolved out by the interferometer.

3.3. Kinematic Structure

Figures 6 and 7 show the velocity and linewidth maps of N_2D^+ and N_2H^+ 3-2. The line velocity was determined through fits of the hyperfine structure of each line using the hfs method in CLASS³, which performs a simultaneous fitting of all hyperfine components using CERN’s “Function Minimization and Error Analysis” package MINUIT⁴. MINUIT has been shown to produce accurate values for line velocities and widths, even in the case of severe line overlap (Pon et al. 2009). Typical uncertainties reported by CLASS for the fits reported here are $\lesssim 0.01 \text{ km s}^{-1}$ in velocity and $\lesssim 0.02 \text{ km s}^{-1}$ in line-width, for N_2H^+ , and $\lesssim 0.01 \text{ km s}^{-1}$ in velocity and $\lesssim 0.03 \text{ km s}^{-1}$ in line-width, for N_2D^+ .

There is very little variation in line center velocity across the N_2D^+ 3-2 map (Fig. 6a), with a possible hint of a gradient across the long axis in the southern part of the core. The variation in line center velocity is mostly $< 0.1 \text{ km s}^{-1}$, larger than the typical uncertainty from hyperfine fitting, and of the same order as the channel separation. The two integrated line peaks have velocities that are separated by about a line width ($\sim 0.25 \text{ km s}^{-1}$). The

³<http://www.iram.fr/IRAMFR/GILDAS>

⁴<http://wwwasdoc.web.cern.ch/wwwasdoc/minuit/minmain.html>

results are similar for N_2H^+ 3-2, in that there is very little variation in line center velocity across the map, with the largest variation occurring along the western edge.

DAM04 found that the linewidth of N_2H^+ 1-0 over N6 is generally $\leq 0.3 \text{ km s}^{-1}$ with a mean value of 0.25 km s^{-1} , with typical uncertainties of $0.005\text{-}0.01 \text{ km s}^{-1}$. Our observations with higher angular resolution confirm this result, and suggest that the linewidth varies by less than the channel width of the observations over most of the map where significant emission is present (Fig. 7). There is a suggestion of large line widths on the western edge, which may be due to the nearby dust continuum source SM2, or simply due to lower S/N in the edges of the map. There appears to be an increase in N_2H^+ line width of order $\sim 0.03\text{--}0.04 \text{ km s}^{-1}$ near the N_2D^+ SE peak, which is also near the position of the continuum source (Fig. 7). This increase is seen in the N_2D^+ data (Figure 8), as the line width of the SE peak of N_2D^+ ($0.279 \pm 0.018 \text{ km s}^{-1}$) is significantly larger than that of the NW peak ($0.217 \pm 0.015 \text{ km s}^{-1}$). As in the case of N_2H^+ 1-0 (DAM04), the observed line width across N6 in the 3-2 lines of N_2H^+ and N_2D^+ is $\sim 0.25 \pm 0.02 \text{ km s}^{-1}$. Observations of the (1,1) and (2,2) lines of NH_3 indicate a gas temperature of $20 \pm 2 \text{ K}$ (Pon et al. 2009). Using this gas temperature, the thermal velocity dispersion σ_{T} is 0.26 km s^{-1} , implying that the non-thermal velocity dispersion σ_{NT} is $\sim 0.08 \text{ km s}^{-1}$. Thus the non-thermal motions within N6 are highly subsonic, with $\sigma_{\text{NT}}/\sigma_{\text{T}} \sim 0.3$.

4. Analysis

4.1. N_2H^+ and N_2D^+ Column Density

Line optical depths (τ) and excitation temperatures (T_{ex}) were determined from fits to the hyperfine components of each transition, using the fitting routines in CLASS (DAM04). CLASS provides an estimate of the optical depth, and the product $[J_{\nu}(T_{\text{ex}}) - J_{\nu}(T_{\text{bg}})]\tau$, where $J_{\nu}(T_{\text{ex}})$ and $J_{\nu}(T_{\text{bg}})$ are the equivalent Rayleigh-Jeans excitation and background temperatures. The method of Caselli et al. (2002b; their appendix, in particular equation (A4)) was used to determine the column density of N_2H^+ and N_2D^+ by integrating over the hyperfine features. This method assumes that the line emission is optically thin. Equation (A4) from Caselli et al. (2002b) is repeated here, as it is important for the following discussion,

$$N_{\text{tot}} = \frac{8\pi W}{\lambda^3 A} \frac{g_l}{g_u} \frac{1}{J_{\nu}(T_{\text{ex}}) - J_{\nu}(T_{\text{bg}})} \frac{1}{1 - \exp(-h\nu/kT_{\text{ex}})} \frac{Q_{\text{rot}}}{g_l \exp(-E_l/kT_{\text{ex}})}, \quad (1)$$

where N_{tot} is the total column density, W is the integrated line emission, λ and ν are the wavelength and frequency of the observations, A is the Einstein coefficient, g_l and g_u are

the statistical weights of the lower and upper levels, and Q_{rot} is the partition function.

Fits to the hyperfine structure of N_2D^+ 3-2 show that this line is optically thin at most positions (but with CLASS usually reporting values > 0.1), with the largest total opacities measured near to the map center at $\tau \sim 2 - 3$. Positions where the total optical depth was ≥ 1 were used to estimate a single excitation temperature for the whole map, for which we find $T_{\text{ex}} = 10.0 \pm 3.3$ K, so we assume a constant T_{ex} of 10 K for N_2D^+ . For N_2D^+ , the total integrated line emission and T_{ex} were used to calculate the column density N at each map position. The results are shown in Figure 9(a). The column density of N_2D^+ ranges from $9.8 \times 10^{11} \text{ cm}^{-2}$ to $4.7 \times 10^{12} \text{ cm}^{-2}$, with values greater than $2 \times 10^{12} \text{ cm}^{-2}$ over much of the map.

The N_2H^+ 3-2 emission was found to be very optically thick over much of N6, making it difficult to estimate τ , and thus determine T_{ex} . In addition, the saturated lines means that the observed integrated line emission is only a lower limit of the true emission, and equation (1) is not valid for optically thick emission. To overcome this problem, a multistep approach was used to obtain an estimate of T_{ex} and measure the integrated line emission, so that the column density could be determined. Most of the optical depth of N_2H^+ 3-2 is due to the main-V hyperfine group. The low-V and high-V groups only account for 0.0742 of the total line strength (normalized to 1.0; Daniel et al. 2006; Pagani, Daniel, & Dubernet 2009). The total integrated line emission was thus found by integrating only over the low-V ($0.22 - 1.58 \text{ km s}^{-1}$) and high-V ($5.07 - 6.18 \text{ km s}^{-1}$) hf groups, and scaling by the inverse of their relative line strength. In the outer part of the N_2H^+ map, the total optical depth drops to reasonable values (< 15), allowing the total line emission to be measured, and compared to the value obtained using only the low-V and high-V hf groups scaled by $1/0.0742$. At these positions, the results were found to be in general agreement (better than 20%). Although the total optical depth is high, the individual hyperfine features are optically thin (39 hyperfine features in total, 17 in the low-V and high-V hyperfine groups), and the total optical depth of the low-V and high-V hf groups together are also thin in these data, or at most $\tau \sim 2$ with an uncertainty of similar size.

While it was possible to obtain good fits to essentially every map position using only the low-V and high-V hf groups, in most cases this resulted in an optically thin fit ($\tau = 0.1$ in CLASS), so that T_{ex} is unconstrained. In order to obtain an estimate of T_{ex} , full hf fitting is needed. Using only those positions away from the map center where the full hf fit gives $\tau < 20$, we obtain $T_{\text{ex}} = 10.0 \pm 2.2$ K. A full hf fit to a spectrum generated from the inner 8×10 positions, gives a similar result. As we were unable to obtain a reliable estimate for each individual map position, we assume that $T_{\text{ex}} = 10 \pm 2$ K across the whole map. This value is significantly lower than the value of 17 K determined by DAM04 for N_2H^+ 1-0, and

the value of the kinetic temperature of 20 K. This difference could suggest that while the 1-0 line is thermalized, the 3-2 line is not. Alternatively, the denser interior of the core, better traced by the 3-2 line, could be colder. However, T_{ex} is fairly constant over the region mapped in N_2H^+ 3-2, and the temperature derived from dust observations is closer to 20 K, so this alternative is the less likely of the two possibilities.

To determine the N_2H^+ 3-2 column density, we assumed that the total column density $N_{\text{tot}} = N_{\text{hf}}/0.0742$, where N_{hf} is the column density of the outer hyperfines, calculated using the integrated line emission of the low-V and high-V hyperfine groups, and assuming a constant T_{ex} of 10 K. As shown in equation (1), the column density N (whether N_{tot} or N_{hf}) is simply a function of T_{ex} , $f(T_{\text{ex}})$, times the integrated line intensity, W , so that $N = W \times f(T_{\text{ex}})$. The column density of N_2H^+ determined in this manner ranges from $3.5 \times 10^{12} \text{ cm}^{-2}$ to $4.6 \times 10^{13} \text{ cm}^{-2}$, with most values being greater than 10^{13} cm^{-2} , and with a significant fraction of the inner map region having values $> 2.5 \times 10^{13} \text{ cm}^{-2}$ (Figure 9(b)). The typical uncertainty in a particular measurement of the column density is $N_{-50\%}^{+100\%}$. Similar values for the N_2H^+ column density were found by DAM04.

We have checked our results, using the outer hyperfine satellite groups and assuming optically thin emission, against N_2H^+ column densities determined from hyperfine fits to the full hyperfine spectra (Caselli et al. 2002b; Di Francesco et al. 2004; Friesen et al. 2010a). We find that the results are consistent, in that the values from the full fit are within the uncertainties of the method we have used. However, N determined from the full fit case are typically, but not systematically, higher (but are sometimes lower) by up to 50%. Because the total optical depth is so high its actual value is not well constrained by the full fit at any particular position, so we prefer the method we have used for estimating N .

4.2. Deuterium Fraction

The ratio of N_2H^+ and N_2D^+ column densities can be used to estimate the deuteration fraction within N6. This is shown in Figure 10, where the ratio $N(\text{N}_2\text{D}^+)/N(\text{N}_2\text{H}^+)$ is shown, compared to the integrated intensity maps of each molecule. From this Figure it can be seen that the D/H ratio is of order 0.05 over a large fraction of the map, reaching higher values toward the western side, of order 0.15. These values are larger than those determined by Pon et al. (2009), from lower resolution observations. Figure 10 also shows that the NW N_2D^+ peak has a higher D/H ratio than the SE peak, as might be expected from Pon et al. (2009), where only the NW peak is clearly detected in the JCMT data. This result shows that Oph A-N6 has a high central degree of deuteration, and is similar to values found for isolated low-mass starless cores (Crapsi et al. 2005). In some map locations the D/H value

is close to the dividing line of 0.1 used to characterize the isolated cores as prestellar or starless, with the idea that prestellar cores are those closest to star formation (Crapsi et al. 2005). Of the prestellar cores identified by Crapsi et al. (2005), all but one, like OphA-N6, have $N(\text{N}_2\text{H}^+) > 10^{13} \text{ cm}^{-2}$. It is notable that even though the kinetic temperatures are near to 20 K, where the D/H ratio should decrease dramatically (Caselli et al. 2008), and significantly higher than in isolated cores, the D/H ratio is as high as in most starless cores, if not higher.

4.3. Structure & Mass

N6 is elongated and may represent a fragment of a filament. The simplest model of a filament is a self-gravitating isothermal cylinder, whose radial density profile is (Ostriker 1964; Johnstone et al. 2003),

$$n(r) = \frac{n_0}{\left[1 + \left(\frac{r^2}{8H^2}\right)\right]^2}, \quad (2)$$

where n_0 is the peak number density, r is the radial offset, and the scale length H is

$$H^2 \equiv \frac{c^2}{4\pi G \rho_0}, \quad (3)$$

where c is the sound speed, ρ_0 the peak density, and G is the gravitational constant.

If N6 is viewed perpendicular to its axis, then the column density along the line-of-sight is

$$N(r) = \frac{\pi}{2} \frac{n_0 H}{\left[1 + \left(\frac{r^2}{8H^2}\right)\right]^{3/2}} \quad (4)$$

$$= N_0 \frac{\pi}{4R} \frac{H}{\left[1 + \left(\frac{r^2}{8H^2}\right)\right]^{3/2}} \quad (5)$$

where N_0 is the peak column density and R is the radius.

Figure 12 shows the radial column density profile across the minor axis of N6 derived from N_2H^+ 3-2 compared to the profile of an isothermal cylinder (dark continuous curve).

This profile was constructed from N_2H^+ 3-2 data imaged with a $2''.4$ beam and $1''.2$ pixels (Nyquist sampling), using the method of “super-resolution” (Briggs 1994; Chandler et al. 2005), in order to better sample the radial profile. Eighteen independent, consecutive profiles were extracted across the major axis at $1''.2$ intervals along the major axis. The region over which the profiles were extracted is shown in Figure 11. Each profile was normalized to its peak values, and the normalized profiles averaged together to form the composite profile shown in Figure 12. This figure shows that the column density profile of N6 is very well represented by an isothermal cylinder, as the model matches the data within its 1σ uncertainties at eight consecutive positions across the peak of the profile. The model allows the peak density and hence abundance of N_2H^+ to be estimated, keeping other parameters fixed at their previously determined values; radius $R = 800$ AU, temperature of 20 K (Pon et al. 2009), and peak N_2H^+ column density of $4.6 \times 10^{13} \text{ cm}^{-2}$. Using these values, we find a good match to the data, as shown in Figure 12, assuming a constant N_2H^+ abundance $X_{\text{N}_2\text{H}^+} = 2.7 \pm 0.2 \times 10^{-10}$, resulting in values of peak density $n_0 = 7.1_{-0.5}^{+0.6} \times 10^6 \text{ cm}^{-3}$, and scale length $H = 362_{-14}^{+12}$ AU. Allowing for a 5 pc uncertainty in the distance does not change these values.

Even though N6 is not a local dust emission peak, DAM04 estimated the column density, $N(\text{H}_2)$, to be $3 \times 10^{23} \text{ cm}^{-2}$ using the dust continuum emission, assuming isothermal dust at a temperature of 20 K. From this and their value for $N(\text{N}_2\text{H}^+)$ they infer an abundance $X(\text{N}_2\text{H}^+)$ of 3×10^{-10} , in very close agreement with the value used here that provides an excellent match between the isothermal cylinder model and the data. This abundance is in good agreement with values inferred for isolated low-mass cores, including the evolved prestellar cores discussed above (Benson, Caselli & Myers 1998; Caselli et al. 2002c; Crapsi et al. 2005).

The mass per unit length of an isothermal cylinder is

$$M(r) = 2\pi\rho_0 \int_0^R r dr \left[1 + \left(\frac{r^2}{8H^2} \right) \right]^{-2} \quad (6)$$

After integrating, the mass of a cylinder of length L can be written:

$$M = L \frac{2c^2}{G} \left[1 + \left(\frac{2c^2}{\pi G \rho_0 R^2} \right) \right]^{-1}. \quad (7)$$

For $T = 20$ K, $n_0 = 7.1 \times 10^6 \text{ cm}^{-3}$, $R = 800$ AU, and $L = 3100$ AU, the mass is $M = 0.18 \pm 0.02 M_\odot$, where the uncertainty is due to the uncertainties in n_0 given above and the distance uncertainty.

We can determine the total mass traced by N_2H^+ , using the N_2H^+ column density map (Fig. 9(b)), with the result for the N_2H^+ abundance. The map gives the column density per pixel, from which the mass per pixel (M_p) can be determined, and hence the total mass, using

$$M_p = X \mu_m A_p N_X , \quad (8)$$

where μ_m is the mean particle mass (2.37 amu; Stahler & Palla 2005; Kauffmann et al. 2008), A_p is the area per pixel, X is the abundance of the molecule used, and N_X is its column density. In a Nyquist sampled map, the total mass is then just the sum over all pixels. For $T_{\text{ex}} = 10$ K and $X_{\text{N}_2\text{H}^+}$ of 2.7×10^{-10} , we measure $M = 0.29^{+0.05}_{-0.04} M_\odot$ for positions within the half-power level of the column density map. The uncertainties come from the uncertainties in X and the distance. The change in mass by assuming $T_{\text{ex}} = 9$ or 11 K is much smaller than either of these.

The critical mass is the mass of a condensation whose radius is equal to the shortest wavelength of a periodic perturbation that will grow. Larson (1985) has studied the critical mass for fragmentation of a number of geometries, and for an isothermal filament (i.e., a cylinder) finds (Larson 1985, equation 21)

$$M_c = \frac{7.88c^4}{G^2\mu_m N} \quad (9)$$

$$= 1.1 \left(\frac{T}{20 \text{ K}} \right)^2 \left(\frac{10^{23} \text{ cm}^{-2}}{N} \right) [M_\odot]. \quad (10)$$

With $T = 20$ K and $N = 1.7 \times 10^{23} \text{ cm}^{-2}$ (from the peak N_2H^+ column density and X), $M_c = 0.63^{+0.05}_{-0.04} M_\odot$. This value is within about a factor of 2 of the mass computed for N6 of $0.29 M_\odot$ from eqn. (8). Given the uncertainties in computing masses, such as determining the “size” of a core, and our method of measuring N at each position, this result suggests that N6 is consistent with having formed from the fragmentation of an isothermal filament, in this case Oph A.

5. Discussion

5.1. Kinematics

Internally, Oph A-N6 is rather quiescent. It shows very narrow N_2H^+ and N_2D^+ line-widths of about 0.25 km s^{-1} across its extent, barely more than the thermal line width for the measured gas temperature of 20 K, of 0.18 km s^{-1} . Its non-thermal motions are very sub-sonic, but the surrounding gas shows significantly larger line-widths (DAM04; André et al. 2007; Pon et al. 2009) suggesting that N6 has lost any turbulent motions it may have had. The lack of significant variation in line centroid velocity and line-width over the core indicate that N6 is an example of a coherent core, as has been seen in more isolated cores (Barranco & Goodman 1998; Goodman et al. 1998; Caselli et al. 2002a; Tafalla et al. 2004; Pineda et al. 2010). This result suggests that small non-thermal motions typical of isolated cores are found in some starless cores within turbulent molecular clouds.

Observations of HCO^+ and DCO^+ 3-2 show the expected signature of inward motions (Evans 1999; Pon et al. 2009), but the complex hyperfine structure of N_2H^+ and N_2D^+ 3-2 makes identifying any similar signature in these lines impossible. In addition, the very narrow line widths of N_2H^+ 1-0 together with the spectral resolution and signal-to-noise of the data make it difficult to identify any signature of inward motions (DAM04), regardless of the hyperfine structure. Data with finer spectral resolution and improved signal-to-noise are required to search for inward motions in N_2H^+ . However, the very narrow line-widths already suggest that any inward motions on the size scales probed by N_2H^+ ($\sim 300 \text{ AU}$) must be small. The ratio of non-thermal-to-thermal line-width in N6 is about 0.3, which is lower than observed in most starless dense cores in Perseus (Walsh et al. 2007; H. Kirk et al. 2007; Rosolowsky et al. 2008), for dense cores elsewhere in Ophiuchus (André et al. 2007; Friesen et al. 2009), or for most isolated low-mass dense cores (Myers 1983). Further, the absence of line-broadening toward the center of N6 suggests a lack of a central source. The motions observed in HCO^+ may be infall onto the core, rather than core collapse (Pon et al. 2009).

5.2. Dust Emission

Starless cores are usually defined through observations of the dust continuum or molecular lines in single-dish observations at millimeter wavelengths, with angular resolution $10\text{-}20''$ (typically the line observations are of lower resolution than the continuum). As a result, by definition they generally only show a single peak of emission, and fairly simple structures, being round or elongated with small aspect ratios (less than 2). When observed with an

interferometer, which acts as a spatial filter, many such cores are not detected, or still only appear as single peaks of emission, due to their smooth large-scale structure and lack of significant sub-structure (Williams & Myers 1999; Williams et al. 1999, 2006; Harvey et al. 2003a; Olmi et al. 2005; Schnee et al. 2010). Combining the single-dish and interferometer line data, as we have done here, allows the small scale structure to be studied, without concerns about missing flux. These studies usually show that starless cores do not break up into sub-cores on small scales. One exception is L183, which is composed of 3 sub-cores in N_2H^+ 1-0 (J. Kirk et al. 2009), but it shows a very elongated structure in single dish maps, so perhaps this is not too surprising.

The nature of the compact dust emission detected toward the peak of integrated N_2H^+ emission is unclear, given that N6 is not a local maximum in single-dish continuum observations between 1300 and 450 μm , with 10-15'' resolution (Motte et al. 1998; Wilson et al. 1999; Johnstone et al. 2000). However, a dust temperature map derived from the ratio of 450-to-850 μm flux, assuming a constant dust emissivity, shows a similar structure to the N_2H^+ maps, although with lower resolution (Pon et al. 2009). The dust temperature map shows a peak of 20 K at the N_2H^+ peak, and is elongated in the NW-SE direction. It is not yet known if the gas temperature varies in a similar manner on similar scales, as the NH_3 observations only have a resolution of about 30''. However, NH_3 may not probe the highest densities toward the center of N6, and so determining the gas temperature there with confidence will be difficult. Supporting evidence for a relatively constant gas temperature within N6 comes from the comparison of its column density profile with that of an isothermal cylinder (Fig. 12), and from the almost constant line-widths.

N6 is embedded within the Oph A ridge, and the large column of dust due to the ridge may make it difficult to distinguish a compact core within it as a separate entity. The dust temperature map suggests that it is a local temperature maximum, at about 20 K (Pon et al. 2009). This result is unlike those in detailed studies of isolated starless cores, which show flat temperature profiles in low-resolution observations (Jijina et al. 1999; Tafalla et al. 2004), but a drop in temperature toward the core center in observations with finer resolution (Crapsi et al. 2007). The mass of dust seen in N6 is very low, only of order 0.005-0.01 M_\odot , and the inferred peak column density of $\sim 1.3 \times 10^{22} \text{ cm}^{-2}$ is an order of magnitude below that found from N_2H^+ observations, and from single-dish continuum observations.

Recently, interferometers have detected compact millimeter dust emission toward three “starless” cores (Chen et al. 2010; Enoch et al. 2010; Pineda et al. 2011; Dunham et al. 2011). Supporting evidence, in the form of CO outflows or faint, compact 70 μm emission, and SED modeling, suggests that in all cases the emission is due to an internal heating source of very low temperature (>100 K), and the inferred luminosities are very low ($<0.1 L_\odot$).

These cores are all candidates to be the long theorized first hydrostatic core (FHSC; Larson 1969; Boss & Yorke 1995; Omukai 2007; Tomida et al. 2010), although none are in complete agreement with theoretical predictions. They have outflows that are too fast (L1448-IRS2E – Chen et al. 2010), too collimated ((L1448-IRS2E – Chen et al. 2010; Per-Bolo 58 – Dunham et al. 2011), or are detected at too short a wavelength (Per-Bolo 58 – Enoch et al. 2011), to be consistent with current models. For one source, L1451-mm, the observations are in better agreement with theoretical models, but a model of a protostar plus a disk provides an equally good fit to its SED and continuum interferometric visibilities (Pineda et al. 2011). Theoretically, a FHSC is expected to be of low mass, with a maximum value of order $0.05 M_{\odot}$, essentially undetectable at $< 100 \mu\text{m}$, and with an observed SED resembling a blackbody at 30 K (Omukai 2007; Saigo & Tomisaka 2011). A low-velocity, compact outflow may also be present. Due to crowding, it is difficult to determine if $70 \mu\text{m}$ Spitzer emission is present toward N6, and as stated it does not show a local maximum in $450\text{-}1300 \mu\text{m}$ emission in single-dish observations. Observations to search for the presence of an outflow in CO 2-1 are compromised by the bright outflow from VLA 1623 (André et al. 1990), that passes close to N6 and is detected in the SMA observations presented here. The compact 1 mm dust emission detected with the SMA has the right mass to be considered a candidate FHSC, but further evidence is needed, particularly detections at other wavelengths. At present there is insufficient information to suggest whether N6 is a better FHSC candidate than the other candidates.

5.3. Comparison to other Starless Cores

Studies of starless cores with resolution similar to the one presented here are rare, particularly in molecular lines. This is a greater problem for cores in clusters, which are typically smaller than more isolated cores, such as those in Taurus (Ward-Thompson et al. 2007, and references therein). Studies with $10\text{-}15''$ resolution have been made for the cluster-forming regions in Ophiuchus (125 pc; Motte et al. 1998; Johnstone et al. 2000; DAM04; Simpson et al. 2008; Friesen et al. 2009), Perseus (~ 235 pc; Hatchell et al. 2005; Walsh et al. 2007) and Serpens (>300 pc; Testi & Sargent 1998; Williams & Myers 1999), and for isolated cores in Taurus (140 pc; Ward-Thompson et al. 1994; Caselli et al. 2002a,b; Tafalla et al. 2002; J. Kirk et al. 2005). A comparison of the properties of N6 with the cores in these studies shows that N6 is denser than most starless cores, by about an order-of-magnitude (10^7 cm^{-3} cf. 10^6 cm^{-3}). These observations typically do not have the resolution of our observations of N6, and derived average densities of 10^6 cm^{-3} over the central 1000 AU could be consistent with peak densities of $\sim 10^7 \text{ cm}^{-3}$ (Keto & Caselli 2010).

N6 is smaller than most cores in all three cluster-forming regions listed above, (Walsh et al. 2007; Friesen et al. 2009), but this could be partly an effect of resolution, as this study has finer resolution by at least a factor of two over previous work. The small size could also be partly due to the molecular transition used, as we have used higher J transitions that preferentially trace higher column density material. Walsh et al. (2007) list a few cores with sizes comparable to N6, but these are at the limit of their resolution. N6 is significantly smaller than all isolated cores that have been well resolved, whether studied in line-emission, dust continuum, or extinction (Ward-Thompson et al. 1999; Bacmann et al. 2000; Crapsi et al. 2005; Kandori et al. 2005; Kauffmann et al. 2008).

As noted earlier, the N_2H^+ linewidths in N6 are narrower than almost all other cluster cores (André et al. 2007; Walsh et al. 2007; H. Kirk et al. 2007; Friesen et al. 2010a), and are almost totally due to thermal motions (as discussed in detail in DAM04). The linewidth barely varies across N6, and it is an excellent example of a coherent core, a core where the non-thermal motions are subsonic, and constant, so that it appears to be cut-off from the surrounding turbulent gas (Mouschovias 1991; Myers 1998; Barranco & Goodman 1998; Goodman et al. 1998; Caselli et al. 2002c; Pineda et al. 2010).

The N_2H^+ column density in N6 is larger than most cores elsewhere in Ophiuchus (Friesen et al. 2010a) and Perseus (H. Kirk et al. 2007), with a peak value of $\sim 5 \times 10^{13} \text{ cm}^{-2}$ compared to values of $\sim 10^{13} \text{ cm}^{-2}$. This peak value is about three times greater than the peak value observed in a sample of 28 isolated starless cores, and about eight times greater than the sample mean ($\sim 8 \times 10^{12} \text{ cm}^{-2}$; Crapsi et al. 2005; see also Daniel et al. 2007). Similarly, the N_2D^+ column density of N6, $\sim 5 \times 10^{12} \text{ cm}^{-2}$, is greater than that of cores in Oph B, where the peak value is $\sim 7 \times 10^{11} \text{ cm}^{-2}$, and greater than the mean value of 25 isolated starless cores, of $< 10^{12} \text{ cm}^{-2}$ (Friesen et al. 2010b; Crapsi et al. 2005; see also Daniel et al. 2007). However, the peak value of $\text{N}(\text{N}_2\text{D}^+)$ for isolated starless cores, observed toward L1544, L429 and L694-2, is similar to N6 (Crapsi et al. 2005).

The deuterium fraction, ranging from a mean near 0.05 to a maximum value of about 0.15, is similar to that seen in 28 isolated cores (range 0.03 – 0.44), where 22 of the cores have $\text{D}/\text{H} < 0.1$ (Crapsi et al. 2005). The range of values in N6 is also similar to that of the cluster-core Oph B2, which has a peak of 0.16 but with most of the core showing values around 0.03 (Friesen et al. 2010b). The mean temperature of the isolated cores is about 10 K, while the mean in Oph B2 is higher at around 13-14 K. The deuterium fraction is expected to be significantly higher in the cold (< 20 K) dense interiors of starless cores than the cosmic D/H ratio. This is due to two main factors. First, the main pathway for the formation of H_2D^+ , the parent molecule of deuterated molecules, is exothermic by 230 K, and the backward reaction is not available. Second, CO will freeze out at temperatures

below 20 K, removing the main destroyer of H_2D^+ . However, N_2 should also freeze out at essentially the same rate as CO at <20 K, so the picture is not so simple. A number of more subtle factors that affect the D/H ratio, such as grain size (surface chemistry), ionization rate, ortho-to-para H_2 value, and the CO depletion factor are examined in detail by Caselli et al. (2008). They show that the D/H ratio can still be relatively high near 20 K, but drops sharply at <15 K. One obvious explanation for the relatively high values of D/H in N6 may be temperatures a few degrees lower than 20 K, but the complete reason for the high D/H values is likely to be more complicated. The D/H ratio is largest away from the dust temperature peak, to the NW, and Pon et al. (2009) do infer a radial temperature drop.

Thus, N6 appears to be denser and smaller than starless cores in both cluster-forming and isolated environments. While a very small number of cluster-cores have a similar size, no isolated core does, and no starless core has a mean density as high.

5.4. Structure and Evolution

Starless cores have typically been modeled with spherically symmetric geometries, with a radial density profile that is almost constant at small radii but decrease as a power law at larger radii (Ward-Thompson et al. 1994, 1999; Bacmann et al. 2000; Evans et al. 2001; Kandori et al. 2005; J. Kirk et al. 2005). However, N6 is clearly elongated, with an aspect ratio of at least 2:1, as observed in many cores (Myers et al. 1991; Ryden 1996), suggesting that it is prolate or filamentary in nature. Over its half-maximum size its dust temperature is fairly uniform at about 20 K, to within 1-2 K, decreasing at larger distances (Pon et al. 2009). We have thus compared the column density profile of N6 to that of an isothermal cylinder (Ostriker 1964; Curry 2000), finding an extremely good match between the data and the model (Fig. 12).

The mass of the isothermal model cylinder is $\sim 0.2 M_\odot$, similar to the observationally derived mass of $0.3 M_\odot$, given the uncertainties in the input values (cylinder size, column density per pixel, temperature). Similarly, the critical mass for fragmentation of an isothermal filament with properties similar to those of N6 is $\sim 0.6 M_\odot$ (Larson 1985), also close to the observational value given the uncertainties (in particular as the observed value of mass depends on column density, whereas the critical cylinder mass depends on its inverse). The excellent match between the column density profile of N6 and the isothermal cylinder model, and the similarity of the observed mass to the mass of an isothermal filament with the properties of N6, strongly suggest that N6 has formed via fragmentation of the Oph A filament, and is in a critical state at the beginning of star formation, or has already started the star-formation process (as evidenced by the low-mass compact dust continuum emission).

N6 is aligned with its parent core, Oph A, supporting the view that it has formed as the result of fragmentation of Oph A along its axis.

Although non-spherically symmetric models are rarely used, they have been quite successful in explaining the observed elongated structure of dense cores and filamentary nature of molecular clouds (Harvey et al. 2003b; Johnstone et al. 2003). It has also been shown that the density profiles of collapsing centrally condensed (“Bonner-Ebert”) spheres and cylinders are remarkably similar, and distinguishing between these cases observationally, using only column density maps, may not be possible (Myers 2005). Resorting to the ease of using spherical models without considering alternatives should be avoided, a message that is often given without heed (Hartmann 2004).

Harvey et al. (2003b) performed a detailed study of the isolated starless core L694-2, through near-infrared extinction mapping. They found that spherical models where the radial density profile is described by a power-law, or a Bonnor-Ebert sphere, did not provide accurate matches to the data. Instead they found that a cylindrical model, like that described here, provided an excellent fit to their data. In the case of L694-2, the cylinder is inclined to the line-of-sight, so initially it was not obvious that a cylindrical model was needed. The steep power-law index that best matched the data, significantly steeper than predicted by inside-out collapse, motivated the cylindrical model.

Many distant infrared dark clouds and nearby star-forming complexes have filamentary or elongated structures (Schneider & Elmegreen 1979; Myers 2009), and in at least one case, that of the infrared dark cloud G11.11-0.12, the radial profile of 850 μm emission closely matches that of an isothermal filament of radius ≈ 0.1 pc over a length of more than 10 pc (Johnstone et al. 2003). While many molecular clouds have been compared to models of infinite or finite sheets, models of individual clouds as cylinders are almost absent, although theoretical studies suggest that such models could provide good matches to available data (Curry 2000). New results from the Herschel Space Observatory show filamentary structures in nearby molecular clouds (André et al. 2010; Arzoumanian et al. 2011), and modelling suggests radial profiles much shallower than isothermal cylinders, at radii > 0.1 pc. At such large radii the assumptions of constant temperature and/or hydrostatic equilibrium are unlikely, so this result is not surprising. The observations do not have the resolution to probe scales similar to that of N6. The profiles could be consistent with collapsing polytropic cylinders (Arzoumanian et al. 2011), or magnetized filaments in virial equilibrium (Fiege & Pudritz 2000). It will be interesting to observe cores within these filaments with finer resolution to study their structure.

The physical, kinematic, and chemical properties of dense cores have been used to assess their evolutionary state (Ward-Thompson et al. 1999; Crapsi et al. 2005; Di Francesco et al.

2007). Crapsi et al. (2005) searched for evolutionary indicators in a sample of 31 isolated cores, using observations of N_2H^+ , N_2D^+ , CO and the dust continuum. They proposed eight chemical and kinematic evolutionary indicators, and identified as “evolved” those cores that met at least four of the conditions. These conditions include large column densities of N_2H^+ and N_2D^+ , a large deuterium fraction, large CO depletion and central density, broad linewidths, infall asymmetry in the line profiles, and compact central regions. All of these conditions, with the exception of CO depletion, can be tested in N6 with our data.

The peak column densities of N_2H^+ ($4.6 \times 10^{13} \text{ cm}^{-2}$) and N_2D^+ ($4.7 \times 10^{12} \text{ cm}^{-2}$) are greater than the dividing values given by Crapsi et al. (2005), of $8.5 \times 10^{12} \text{ cm}^{-2}$ and $1.0 \times 10^{12} \text{ cm}^{-2}$, respectively. Similarly, the peak of the deuterium fraction, 0.15, is greater than the value of 0.1 used by Crapsi et al. to separate candidate prestellar cores from starless cores. The peak density we determine, $7.0 \times 10^6 \text{ cm}^{-3}$, is far greater than the separator of $5.1 \times 10^5 \text{ cm}^{-3}$ used by Crapsi et al., as is the degree of central concentration (this is not a function of resolution, as the single dish data have been included in our results). The narrow line widths, and hyperfine structure, makes the search for line skewness difficult. As mentioned, Pon et al. (2009) observe infall asymmetry in HCO^+ , so there is some evidence of contraction in N6. However, the N_2H^+ and N_2D^+ lines widths are of similar size to the separating value of 0.25 km s^{-1} used by Crapsi et al. (2005). So of the seven evolutionary indicators we can measure, five clearly indicate that N6 is an evolved prestellar core, according to the analysis of Crapsi et al. (2005), while the other two indicators are borderline (line widths) or unclear (infall asymmetry or line skewness). These results strongly suggest that N6 is at an advanced stage of prestellar evolution. The compact dust continuum emission further supports this idea.

6. Summary & Conclusions

We have presented high spatial ($\sim 500 \text{ AU}$) and spectral (0.07 km s^{-1}) resolution observations in N_2H^+ 3-2, N_2D^+ 3-2, and the dust continuum at 1-mm, of the starless core Oph A-N6, embedded within the Oph A molecular ridge in the Ophiuchus cluster-forming molecular cloud. These are the highest resolution observations of a starless dense core presented to date. Such a small condensation as N6 would be hard to detect with coarser angular resolution observations, especially in clouds much more distant than Ophiuchus.

The major results of this study are summarized below:

1. The observations reveal a compact dust continuum peak, of size $\sim 1000 \text{ AU}$ and mass $0.005\text{-}0.01 M_\odot$, not seen in single dish observations, except in a dust temperature map (Pon et al. 2009). The small size and mass suggests it might be the first indication

of collapse, either representing a temperature increase, or possibly a first hydrostatic core.

2. The size of N6 from the line observations is larger, with a projected half-power diameter of 3100×1600 AU, and thus an aspect ratio of 2:1. The N_2H^+ and N_2D^+ integrated line maps show slightly different position angles, probably representing chemical variations, or the very high optical depth in N_2H^+ .
3. Very little variation is seen in either linewidth or line center velocity in either line across their maps. The variations are so small that N6 appears to be a coherent core, with very small non-thermal motions.
4. The peak column densities are $4.6 \times 10^{13} \text{ cm}^{-2}$ for N_2H^+ , and $4.7 \times 10^{12} \text{ cm}^{-2}$ for N_2D^+ . The positions of peak column density are offset, with the N_2D^+ peak located to the NW of the N_2H^+ peak.
5. The deuterium fraction has a peak value of 0.15, and is greater than or about equal to 0.05 over much of the mapped area. The maximum value of deuteration lies in the NW, and not at the position of the dust continuum peak, nor the N_2H^+ peak.
6. The column density profile of N6 across its minor axis, as determined from the N_2H^+ observations, is very well represented by an isothermal cylinder (at 20 K), of peak density $7.1 \times 10^6 \text{ cm}^{-3}$, and N_2H^+ abundance 2.7×10^{-10} .
7. The mass of N6, determined from the mapped positions, lies in the range 0.25-0.34 M_\odot , depending strongly on the assumed N_2H^+ abundance ($2.7 \pm 0.2 \times 10^{-10}$). The low value compares favourably to the mass determined from the cylindrical analysis, of $\sim 0.2 M_\odot$, while the high value compares well to the critical mass for fragmentation of an isothermal filament with similar properties, of $\sim 0.6 M_\odot$.
8. Compared to isolated low-mass cores, Oph A-N6 shows similar narrow line widths and small velocity variation, with a deuterium fraction that is similar to “evolved” dense cores. It is significantly smaller than isolated cores, with larger peak column density and volume density, while the previously measured kinetic temperature is significantly higher than isolated starless cores.

These results strongly suggest Oph A-N6 has formed from the fragmentation of the Oph A filament, and is a precursor to a low-mass star in a cluster-forming region. The results also suggest Oph A-N6 has completed almost all of its prestellar evolution, and may even have begun to form a star.

This research is supported in part by the National Science Foundation under grant number 0708158 (T.L.B.). We thank Andy Pon and Rachel Friesen for sharing results in advance of publication, and Rachel Friesen and Chris de Vries for checking column density estimates for optically thick N_2H^+ . We thank Mark Gurwell for his diligent maintenance of the “Submillimeter Calibrator List”. The Submillimeter Array is a joint project between the Smithsonian Astrophysical Observatory and the Academia Sinica Institute of Astronomy and Astrophysics and is funded by the Smithsonian Institution and the Academia Sinica. The James Clerk Maxwell Telescope is operated by The Joint Astronomy Centre on behalf of the Science and Technology Facilities Council of the United Kingdom, the Netherlands Organisation for Scientific Research, and the National Research Council of Canada. Based on observations carried out with the IRAM 30 m telescope. IRAM is supported by INSU/CNRS (France), MPG (Germany) and IGN (Spain). This research has made use of NASA’s Astrophysics Data System Bibliographic Services

REFERENCES

- Allen, L., Megeath, S. T., Gutermuth, R., et al. 2007, *Protostars and Planets V*, ed. B. Reipurth, D. Jewitt, & K. Keil, (Tucson: University of Arizona Press), 361
- Andre, P., Martin-Pintado, J., Despois, D., & Montmerle, T. 1990, *A&A*, 236, 180
- André, P., Belloche, A., Motte, F., & Peretto, N. 2007, *A&A*, 472, 519
- Arzoumanian, D., André, P., Didelon, P., et al. 2011, *A&A*, 529, L6
- Bacmann, A., André, P., Puget, J.-L., et al., 2000, *A&A*, 361, 555
- Barranco, J. A., & Goodman, A. A. 1998, *ApJ*, 504, 207
- Benson, P. J., Caselli, P., & Myers, P. C. 1998, *ApJ*, 506, 743
- Bonnell, I. A., Bate, M. R., Clarke, C. J., & Pringle, J. E. 2001, *MNRAS*, 323, 785
- Bonnell, I. A., & Bate, M. R. 2006, *MNRAS*, 370, 488
- Boss, A. P., & Yorke, H. W. 1995, *ApJ*, 439, L55
- Bressert, E., Bastian, N., Gutermuth, R., et al. 2010, *MNRAS*, 409, L54
- Briggs, D. S. 1994, in *The Restoration of HST Images and Spectra - II*, ed. R.J. Hanisch, & R.L. White (Baltimore: Space Telescope Science Institute), 250

- Caselli, P., Myers, P. C., & Thaddeus, P. 1995, *ApJ*, 455, L77
- Caselli, P., Walmsley, C. M., Zucconi, A., et al., 2002a, *ApJ*, 565, 331
- Caselli, P., Walmsley, C. M., Zucconi, A., et al., 2002b, *ApJ*, 565, 344
- Caselli, P., Benson, P. J., Myers, P. C., & Tafalla, M. 2002c, *ApJ*, 572, 238
- Caselli, P., Vastel, C., Ceccarelli, C., et al., 2008, *A&A*, 492, 703
- Chandler, C. J., Brogan, C. L., Shirley, Y. L., & Loinard, L. 2005, *ApJ*, 632, 371
- Chen, X., Arce, H. G., Zhang, Q., et al., 2010, *ApJ*, 715, 1344
- Chini, R., Reipurth, B., Ward-Thompson, D., et al., 1997, *ApJ*, 474, L135
- Chini, R., Kämpgen, K., Reipurth, B., et al. 2003, *A&A*, 409, 235
- Crapsi, A., Caselli, P., Walmsley, C. M., et al., 2005, *ApJ*, 619, 379
- Crapsi, A., Caselli, P., Walmsley, M. C., & Tafalla, M. 2007, *A&A*, 470, 221
- Curry, C. L. 2000, *ApJ*, 541, 831
- Daniel, F., Cernicharo, J., & Dubernet, M.-L. 2006, *ApJ*, 648, 461
- Daniel, F., Cernicharo, J., Roueff, E., Gerin, M., & Dubernet, M. L. 2007, *ApJ*, 667, 980
- Davis, C. J., Matthews, H. E., Ray, T. P., Dent, W. R. F., & Richer, J. S. 1999, *MNRAS*, 309, 141
- de Geus, E. J., de Zeeuw, P. T., & Lub, J. 1989, *A&A*, 216, 44
- di Francesco, J., André, P., & Myers, P. C. 2004, *ApJ*, 617, 425 [DAM04]
- di Francesco, J., Evans, N. J., II, Caselli, P., et al., 2007, in *Protostars and Planets V*, ed. B. Reipurth, D. Jewitt, & K. Keil, (Tucson: University of Arizona Press), 17
- Dunham, M. M., Chen, X., Arce, H. G., et al. 2011, arXiv:1108.1342
- Enoch, M. L., Young, K. E., Glenn, J., et al. 2006, *ApJ*, 638, 293
- Enoch, M. L., Glenn, J., Evans, N. J., II, et al., 2007, *ApJ*, 666, 982
- Enoch, M. L., Evans, N. J., II, Sargent, A. I., et al., 2008, *ApJ*, 684, 1240
- Enoch, M. L., Lee, J.-E., Harvey, P., Dunham, M. M., & Schnee, S. 2010, *ApJ*, 722, L33

- Evans, N. J., II 1999, *ARA&A*, 37, 311
- Evans, N. J., II, Rawlings, J. M. C., Shirley, Y. L., & Mundy, L. G. 2001, *ApJ*, 557, 193
- Fiege, J. D., & Pudritz, R. E. 2000, *MNRAS*, 311, 85
- Friesen, R. K., Di Francesco, J., Shirley, Y. L., & Myers, P. C. 2009, *ApJ*, 697, 1457
- Friesen, R. K., Di Francesco, J., Shimajiri, Y., & Takakuwa, S. 2010a, *ApJ*, 708, 1002
- Friesen, R. K., Di Francesco, J., Myers, P. C., et al., 2010b, *ApJ*, 718, 666
- Goodman, A. A., Barranco, J. A., Wilner, D. J., & Heyer, M. H. 1998, *ApJ*, 504, 223
- Gutermuth, R. A., Megeath, S. T., Myers, P. C., et al., 2009, *ApJS*, 184, 18
- Hartmann, L. 2004, in *IAU Symp. 221, Star Formation at High Angular Resolution*, ed. M. Burton, R. Jayawardhana, & T. Bourke, (San Francisco, CA: ASP), 201
- Harvey, D. W. A., Wilner, D. J., Myers, P. C., & Tafalla, M. 2003a, *ApJ*, 597, 424
- Harvey, D. W. A., Wilner, D. J., Lada, C. J., Myers, P. C., & Alves, J. F. 2003b, *ApJ*, 598, 1112
- Hatchell, J., Richer, J. S., Fuller, G. A., et al., 2005, *A&A*, 440, 151
- Hildebrand, R. H. 1983, *QJRAS*, 24, 267
- Ikeda, N., Sunada, K., & Kitamura, Y. 2007, *ApJ*, 665, 1194
- Ikeda, N., Kitamura, Y., & Sunada, K. 2009, *ApJ*, 691, 1560
- Jijina, J., Myers, P. C., & Adams, F. C. 1999, *ApJS*, 125, 161
- Johnstone, D., & Bally, J. 1999, *ApJ*, 510, L49
- Johnstone, D., Wilson, C. D., Moriarty-Schieven, G., et al., 2000, *ApJ*, 545, 327
- Johnstone, D., Fiege, J. D., Redman, R. O., Feldman, P. A., & Carey, S. J. 2003, *ApJ*, 588, L37
- Johnstone, D., Di Francesco, J., & Kirk, H. 2004, *ApJ*, 611, L45
- Jørgensen, J. K., Johnstone, D., Kirk, H., et al., *ApJ*, 683, 822
- Kandori, R., Nakajima, Y., Tamura, M., et al. 2005, *AJ*, 130, 2166

- Kauffmann, J., Bertoldi, F., Bourke, T. L., Evans, N. J., II, & Lee, C. W. 2008, *A&A*, 487, 993
- Keto, E., & Caselli, P. 2010, *MNRAS*, 402, 1625
- Kirk, H., Johnstone, D., & Di Francesco, J. 2006, *ApJ*, 646, 1009
- Kirk, H., Johnstone, D., & Tafalla, M. 2007, *ApJ*, 668, 1042
- Kirk, J. M., Ward-Thompson, D., & André, P. 2005, *MNRAS*, 360, 1506
- Kirk, J. M., Crutcher, R. M., & Ward-Thompson, D. 2009, *ApJ*, 701, 1044
- Knude, J., & Hog, E. 1998, *A&A*, 338, 897
- Lada, C. J., & Lada, E. A. 2003, *ARA&A*, 41, 57
- Larson, R. B. 1969, *MNRAS*, 145, 271
- Larson, R. B. 1985, *MNRAS*, 214, 379
- Larson, R. B. 2003, *Reports on Progress in Physics*, 66, 1651
- Larson, R. B. 2005, *MNRAS*, 359, 211
- Li, D., Velusamy, T., Goldsmith, P. F., & Langer, W. D. 2007, *ApJ*, 655, 351
- Lis, D. C., Serabyn, E., Keene, J., et al., 1998, *ApJ*, 509, 299
- Loinard, L., Torres, R. M., Mioduszewski, A. J., & Rodríguez, L. F. 2008, *ApJ*, 675, L29
- Lombardi, M., Lada, C. J., & Alves, J. 2008, *A&A*, 489, 143
- Maruta, H., Nakamura, F., Nishi, R., Ikeda, N., & Kitamura, Y. 2010, *ApJ*, 714, 680
- Motte, F., Andre, P., & Neri, R. 1998, *A&A*, 336, 150
- Mouschovias, T. C. 1991, *ApJ*, 373, 169
- Myers, P. C. 1983, *ApJ*, 270, 105
- Myers, P. C., Fuller, G. A., Goodman, A. A., & Benson, P. J. 1991, *ApJ*, 376, 561
- Myers, P. C. 1998, *ApJ*, 496, L109
- Myers, P. C. 2005, *ApJ*, 623, 280

- Myers, P. C. 2009, *ApJ*, 700, 1609
- Nutter, D. J., Ward-Thompson, D., & André, P. 2005, *MNRAS*, 357, 975
- Olmi, L., Testi, L., & Sargent, A. I. 2005, *A&A*, 431, 253
- Omukai, K. 2007, *PASJ*, 59, 589
- Ossenkopf, V., & Henning, T. 1994, *A&A*, 291, 943
- Ostriker, J. 1964, *ApJ*, 140, 1056
- Padgett, D. L., et al. 2008, *ApJ*, 672, 1013
- Pagani, L., Daniel, F., & Dubernet, M.-L. 2009, *A&A*, 494, 719
- Pineda, J. E., Goodman, A. A., Arce, H. G., et al., 2010, *ApJ*, 712, L116
- Pineda, J. E., Arce, H. G., Schnee, S., et al. 2011, arXiv:1109.1207
- Pon, A., Plume, R., Friesen, R. K., et al., 2009, *ApJ*, 698, 1914
- Rosolowsky, E. W., Pineda, J. E., Foster, J. B., et al., 2008, *ApJS*, 175, 509
- Ryden, B. S. 1996, *ApJ*, 471, 822
- Saigo, K., & Tomisaka, K. 2011, *ApJ*, 728, 78
- Sandell, G., & Knee, L. B. G. 2001, *ApJ*, 546, L49
- Schnee, S., Enoch, M., Johnstone, D., et al., 2010, *ApJ*, 718, 306
- Schneider, S., & Elmegreen, B. G. 1979, *ApJS*, 41, 87
- Shu, F. H., Adams, F. C., & Lizano, S. 1987, *ARA&A*, 25, 23
- Shu, F. H., Li, Z.-Y., & Allen, A. 2004, in *ASP Conf. Ser. 323, Star Formation in the Interstellar Medium: In Honor of David Hollenbach, Chris McKee and Frank Shu*, ed. D. Johnstone, F.C. Adams, D.N.C. Lin, D.A. Neufeld, & E.C. Ostriker (San Francisco, CA: ASP), 37
- Simpson, R. J., Nutter, D., & Ward-Thompson, D. 2008, *MNRAS*, 391, 205
- Stahler, S. W., & Palla, F. 2005, *The Formation of Stars*, (Wiley-VCH)
- Stanke, T., Smith, M. D., Gredel, R., & Khanzadyan, T. 2006, *A&A*, 447, 609

- Tafalla, M., Myers, P. C., Caselli, P., Walmsley, C. M., & Comito, C. 2002, *ApJ*, 569, 815
- Tafalla, M., Myers, P. C., Caselli, P., & Walmsley, C. M. 2004, *A&A*, 416, 191
- Takakuwa, S., et al. 2007, *ApJ*, 662, 431
- Tan, J. C., Krumholz, M. R., & McKee, C. F. 2006, *ApJ*, 641, L121
- Tatematsu, K., Kandori, R., Umemoto, T., & Sekimoto, Y. 2008, *PASJ*, 60, 407
- Testi, L., & Sargent, A. I. 1998, *ApJ*, 508, L91
- Tomida, K., Machida, M. N., Saigo, K., Tomisaka, K., & Matsumoto, T. 2010, *ApJ*, 725, L239
- van Kempen, T. A., van Dishoeck, E. F., Salter, D. M., et al., 2009, *A&A*, 498, 167
- Vogel, S. N., Wright, M. C. H., Plambeck, R. L., & Welch, W. J. 1984, *ApJ*, 283, 655
- Walsh, A. J., Myers, P. C., Di Francesco, J., et al., 2007, *ApJ*, 655, 958
- Ward-Thompson, D., Scott, P. F., Hills, R. E., & Andre, P. 1994, *MNRAS*, 268, 276
- Ward-Thompson, D., Motte, F., & Andre, P. 1999, *MNRAS*, 305, 143
- Ward-Thompson, D., André, P., Crutcher, R., et al., 2007, in *Protostars and Planets V*, ed. B. Reipurth, D. Jewitt, & K. Keil, (Tucson: University of Arizona Press), 33
- Wilking, B. A., Gagné, M., & Allen, L. E. 2008, in *Handbook of Star Forming Regions*, Volume II, ed. B. Reipurth (San Francisco, CA: ASP), 351
- Williams, J. P., & Myers, P. C. 1999, *ApJ*, 518, L37
- Williams, J. P., Myers, P. C., Wilner, D. J., & di Francesco, J. 1999, *ApJ*, 513, L61
- Williams, J. P., & Myers, P. C. 2000, *ApJ*, 537, 891
- Williams, J. P., Lee, C. W., & Myers, P. C. 2006, *ApJ*, 636, 952
- Wilner, D. J., & Welch, W. J. 1994, *ApJ*, 427, 898
- Wilson, C. D., Avery, L. W., Fich, M., et al. 1999, *ApJ*, 513, L139
- Young, K. E., Enoch, M. L., Evans, N. J., II, et al. 2006, *ApJ*, 644, 326
- Zhang, Q., Ho, P. T. P., & Wright, M. C. H. 2000, *AJ*, 119, 1345

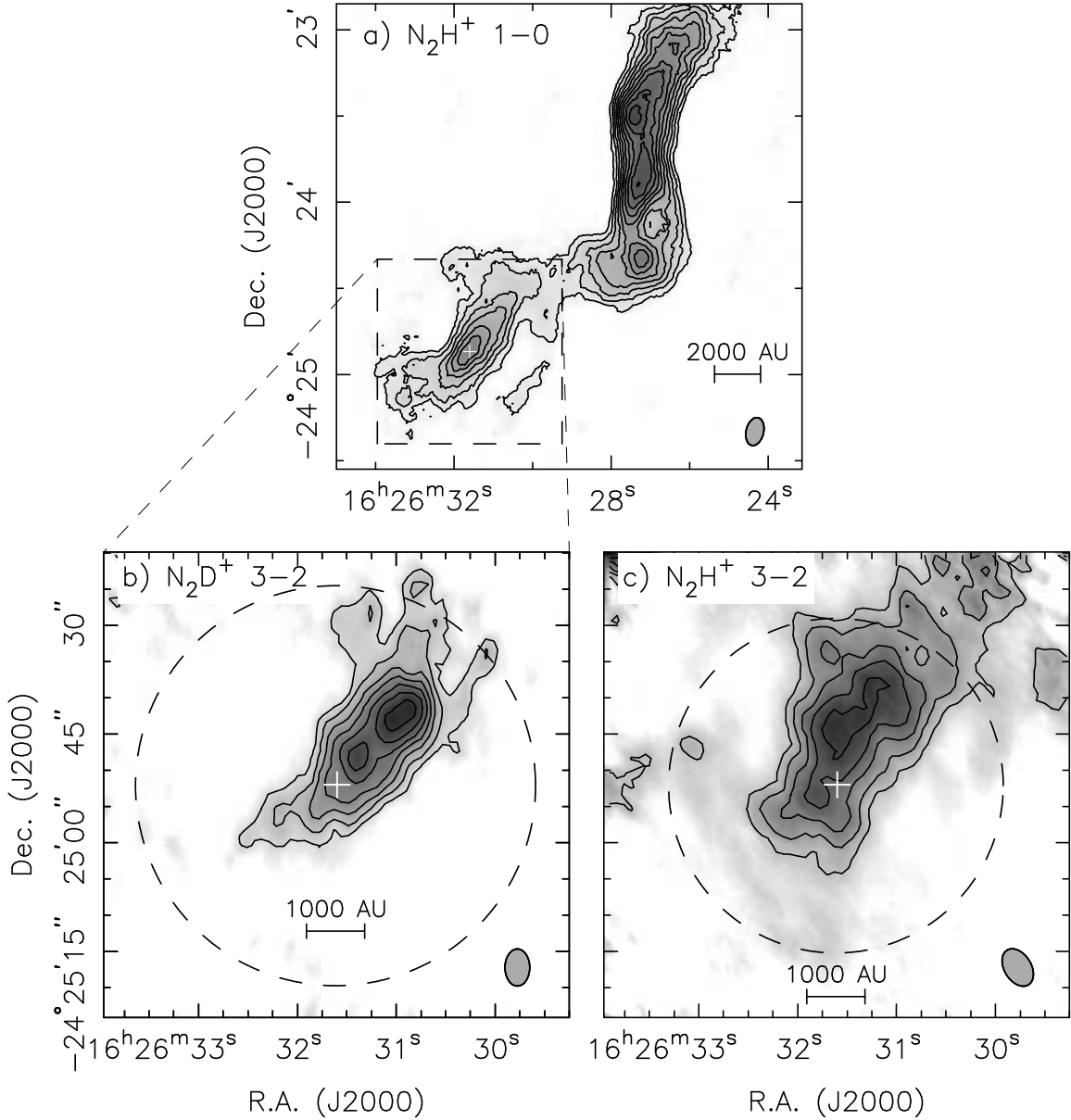


Fig. 1.— Integrated combined single-dish + interferometer line maps of (a) N_2H^+ 1-0 (from DAM04), (b) N_2D^+ 3-2, and (c) N_2H^+ 3-2. The contour levels are (a) 6, 9, 12 ... times the 1σ sensitivity of $0.6 \text{ Jy/beam km s}^{-1}$ for N_2H^+ 1-0, (b) 9, 12, 15 ... times the 1σ sensitivity of $0.12 \text{ Jy/beam km s}^{-1}$ for N_2D^+ 3-2, and (c) 12, 15, 18 ... times the 1σ sensitivity of $0.47 \text{ Jy/beam km s}^{-1}$ for N_2H^+ 3-2. The white cross is the position of the peak integrated N_2H^+ 1-0 emission from DAM04. The large dashed circles in (b) and (c) indicate the size of the SMA primary beam (full-width at half-maximum sensitivity). The small grey ovals at lower right in each panel indicate the synthesised beam sizes (full-width at half-maximum sensitivity).

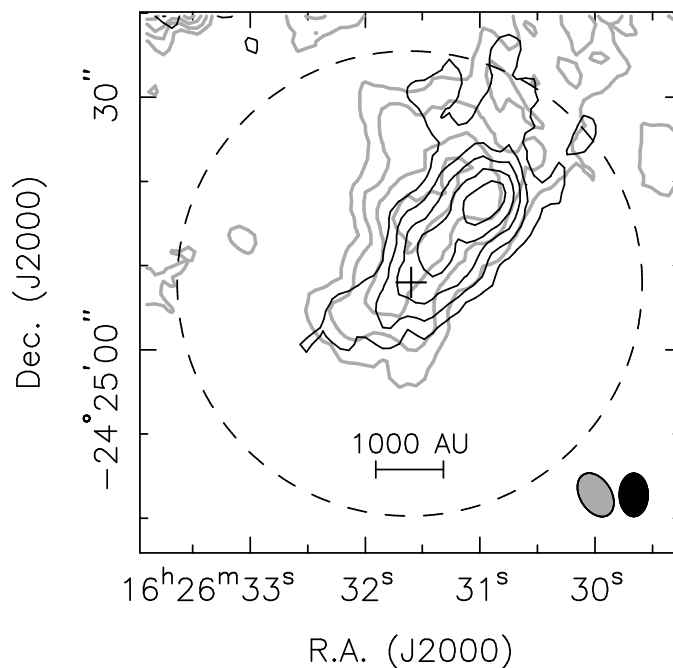


Fig. 2.— Comparison of the integrated line maps of N_2D^+ 3-2 (black contours) and N_2H^+ 3-2 (grey contours). The black cross is the position of the peak integrated N_2H^+ 1-0 from DAM04. The synthesised beam size for each observation is shown in the corresponding colours at lower right, and the primary beam size for the N_2D^+ observations is shown as the dashed circle. Contour levels are 10, 14, 18 ... times the 1σ sensitivity of $0.12 \text{ Jy/beam km s}^{-1}$ for N_2D^+ 3-2, and 12, 16, 20 ... times the 1σ sensitivity of $0.47 \text{ Jy/beam km s}^{-1}$ for N_2H^+ 3-2.

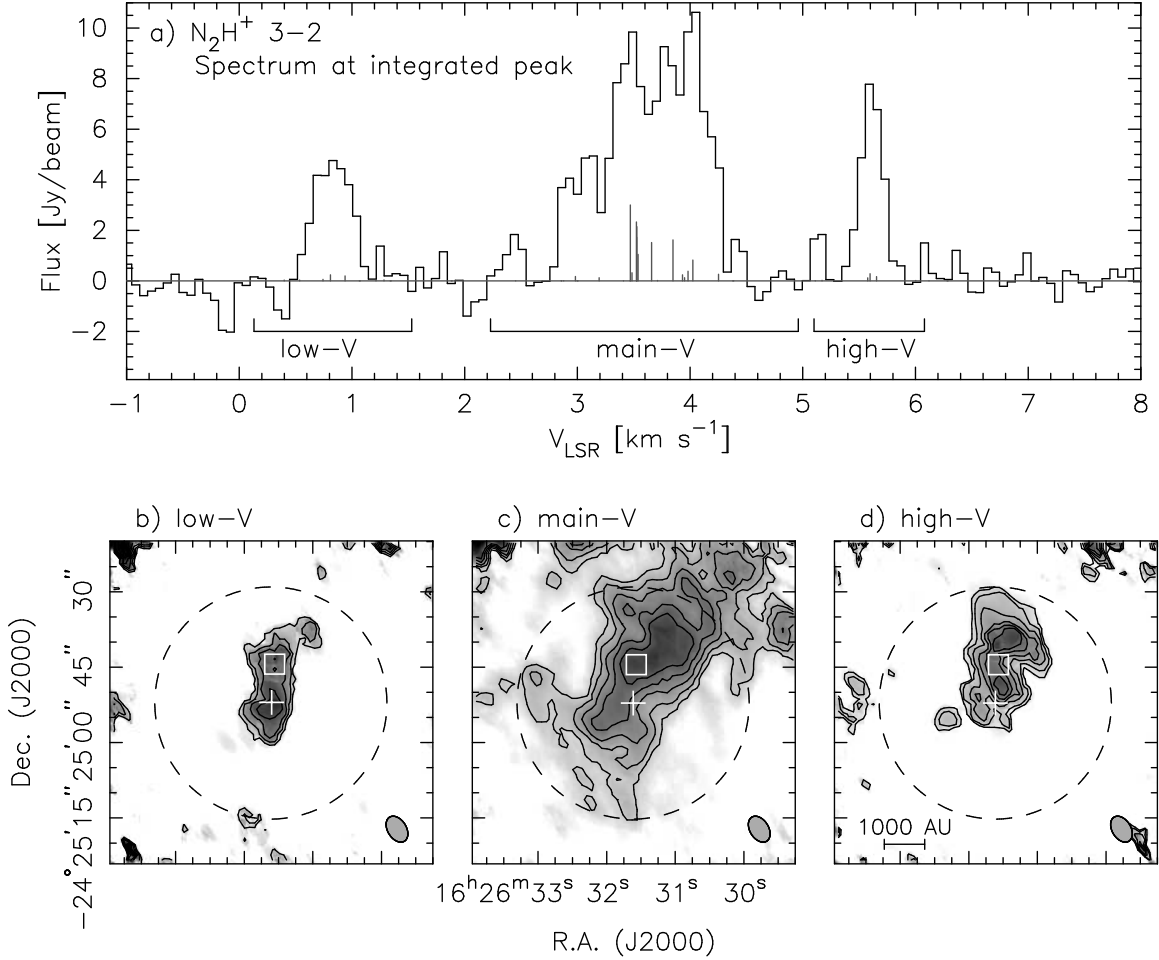


Fig. 3.— Spectrum of N_2H^+ 3-2, panel (a), and maps of integrated N_2H^+ 3-2 emission over the 3 hyperfine groups, panels (b)-(d). Data is combined 30-m + SMA (compact+subcompact). In (a), the location of the hyperfine components, and their relative weights, are indicated by the light grey lines. The limits of integration are indicated by “low-V”, “main-V”, and “high-V”, for panels (b)-(d). The rms noise in the spectrum is 0.5 Jy/beam. Contour levels are (b) 3, 4, 5, ... times the 1σ sensitivity of 0.26 Jy/beam $km\ s^{-1}$, (c) 15, 18, 21, ... times the 1σ sensitivity of 0.30 Jy/beam $km\ s^{-1}$, and (d) 3, 4, 5, ... times the 1σ sensitivity of 0.21 Jy/beam. The white cross is the position of the peak integrated N_2H^+ 1-0 emission (DAM04), while the white square marks the position of the spectrum shown in (a). The large dashed circle indicates the size of the SMA primary beam. The small grey ovals at lower right in panels (b)-(d) indicate the synthesised beam size.

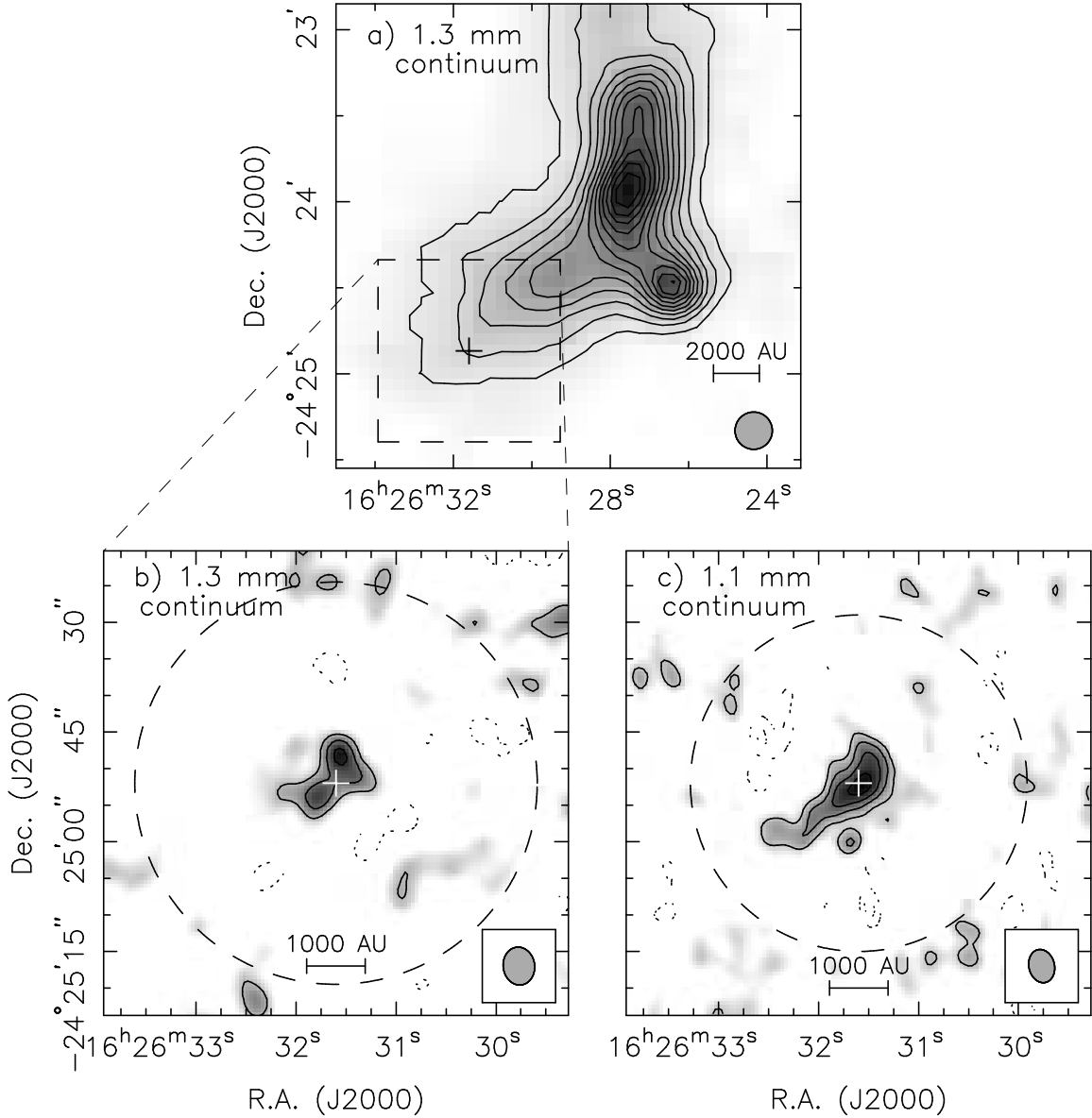


Fig. 4.— Maps of (a) 1.3 mm emission (30-m), (b) 1.3 mm emission (SMA) and (c) 1.1 mm emission (SMA). Contours for (a) the 30-m observations are 10, 20, 30, ... times the 1σ sensitivity of 10 mJy/beam (Motte et al. 1998; DAM04). Contours for the SMA observations are 2, 3, 4, ... times the 1σ sensitivity of (b) 2.6 mJy/beam (1.3 mm) and (c) 3.6 mJy/beam (1.1 mm). Dotted contours indicate negative levels. The cross is the position of the peak integrated N_2H^+ 1-0 emission (DAM04). The large dashed circles indicates the size of the SMA primary beam. The small grey ovals at lower right each panel indicate the synthesised beam size.

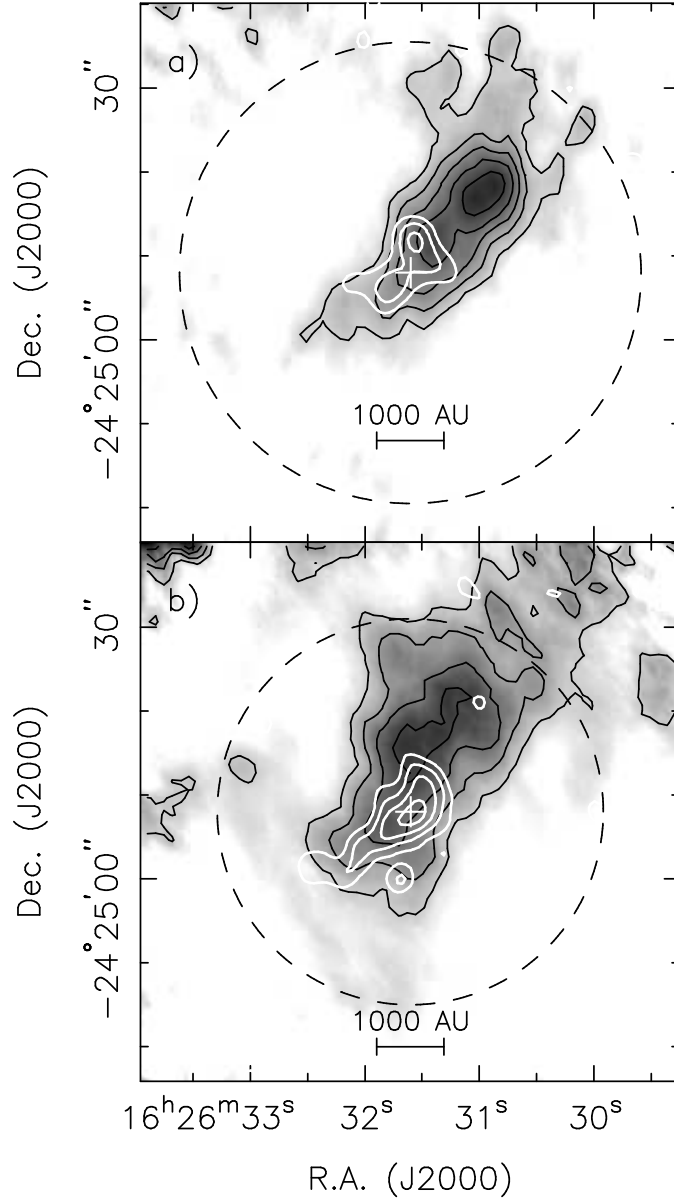


Fig. 5.— Comparison of continuum and integrated line maps. (a) Contours of 1.3 mm continuum emission (white; SMA) over contours of integrated N_2D^+ 3-2 emission (SMA+JCMT). The greyscale is integrated N_2D^+ 3-2 emission. (b) Contours of 1.1 mm emission (SMA) over contours of integrated N_2H^+ 3-2 emission (SMA+30-m). Contour levels for N_2D^+ are 10, 14, 18, ... times the 1σ sensitivity of $0.12 \text{ Jy/beam km s}^{-1}$, while contour levels for N_2H^+ are 12, 16, 20, ... times 1σ sensitivity of $0.47 \text{ Jy/beam km s}^{-1}$. Continuum contour levels are the same as shown in Figures 4(a)–(b). The white cross is the position of the peak integrated N_2H^+ 1-0 emission (DAM04). The primary beam size of the SMA for each observation is shown as the dashed circle.

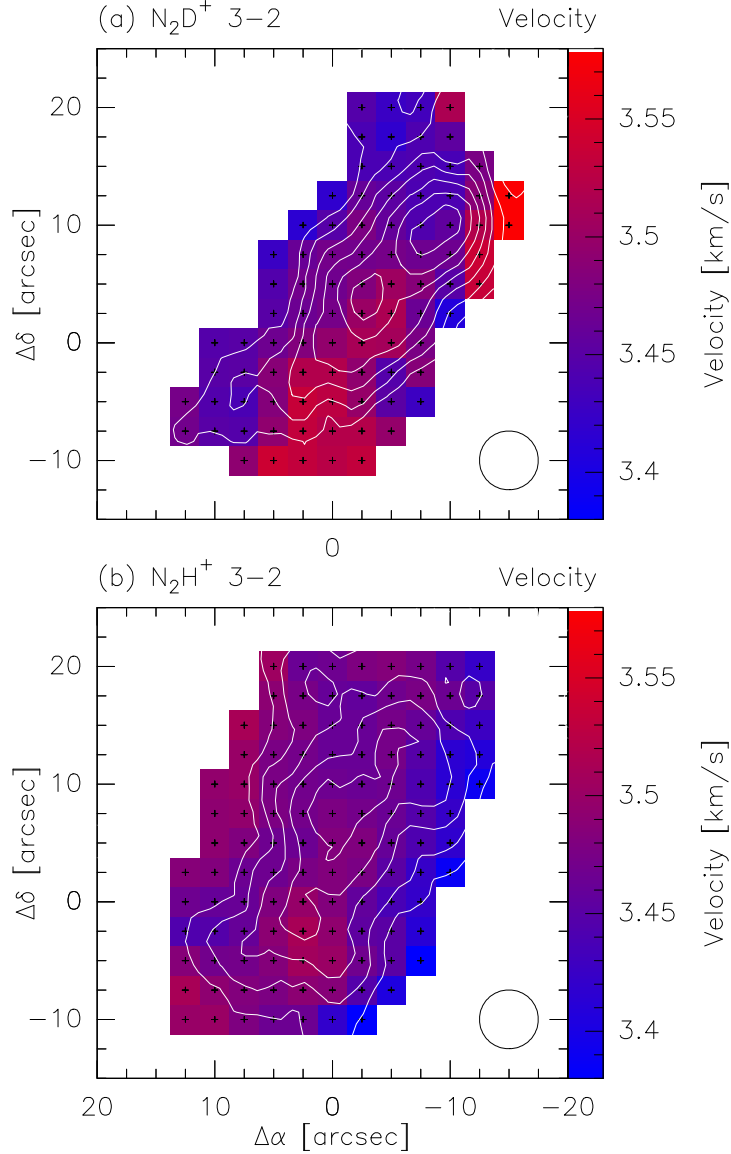


Fig. 6.— (a) Velocity map from hyperfine fits to the N_2D^+ 3-2 data. The data have been resampled onto a $2''.5$ grid with a $5''$ circular beam (shown at lower right). The positions where a fit was performed are indicated by crosses. Typical uncertainties in the fitted velocities are $0.01\text{-}0.02 \text{ km s}^{-1}$. The contours represent the integrated intensity map of N_2D^+ and are the same as shown in Figure 1. (b) Velocity map from hyperfine fits to the N_2H^+ 3-2 data. Typical uncertainties in the fitted velocities are $0.005\text{-}0.02 \text{ km s}^{-1}$. Other details are the same as in (a), except that the contours represent the integrated intensity map of N_2H^+ and are the same as shown in Figure 1. The origin of the maps is the position of the peak integrated N_2H^+ 1-0 emission (DAM04). The open circle indicates the beam size. **[COLOUR FIGURE]**

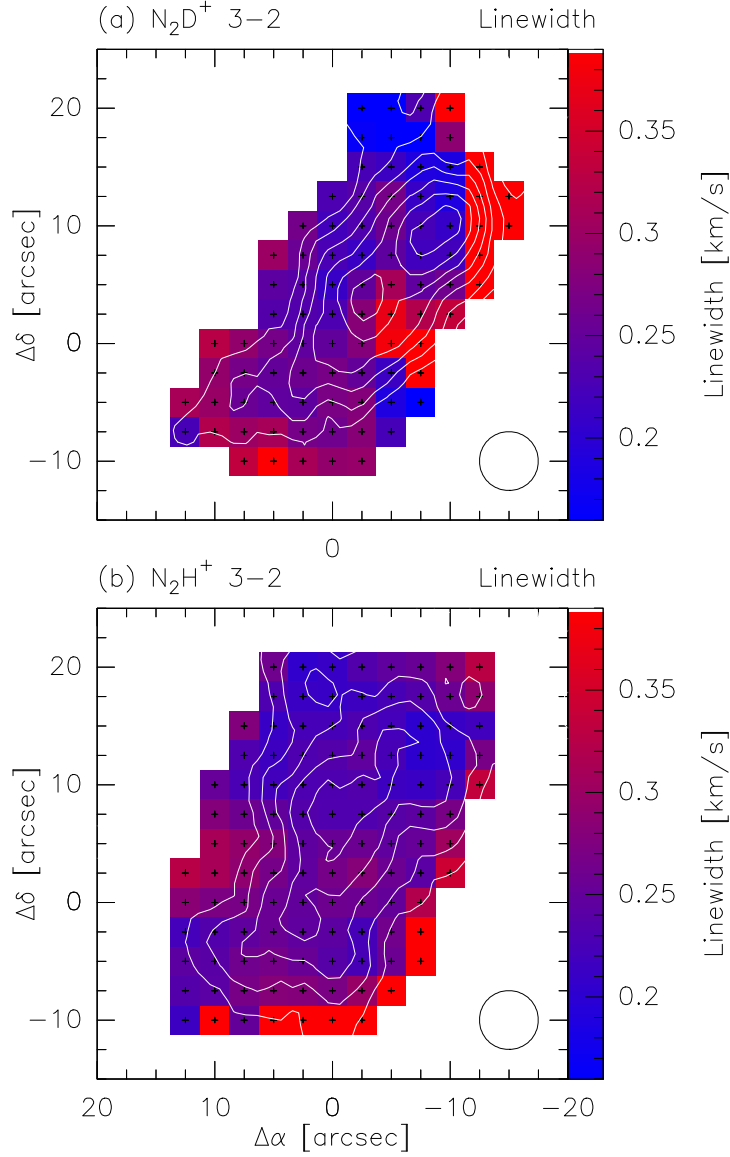


Fig. 7.— (a) Linewidth map from hyperfine fits to the N_2D^+ 3-2 data. The data have been resampled onto a $2''.5$ grid with a $5''$ circular beam (shown at lower right). Typical uncertainties in the fitted linewidths are $0.02\text{-}0.04 \text{ km s}^{-1}$. The positions where a fit was performed are indicated by crosses. The contours represent the integrated intensity map of N_2D^+ and are the same as shown in Figure 1. (b) Linewidth map from hyperfine fits to the N_2D^+ 3-2 data. Typical uncertainties in the fitted linewidths are $0.01\text{-}0.03 \text{ km s}^{-1}$. Other details are the same as in (a), except that the contours represent the integrated intensity map of N_2H^+ and are the same as shown in Figure 1. The origin of the maps is the position of the peak integrated N_2H^+ 1-0 emission (DAM04). **[COLOUR FIGURE]**

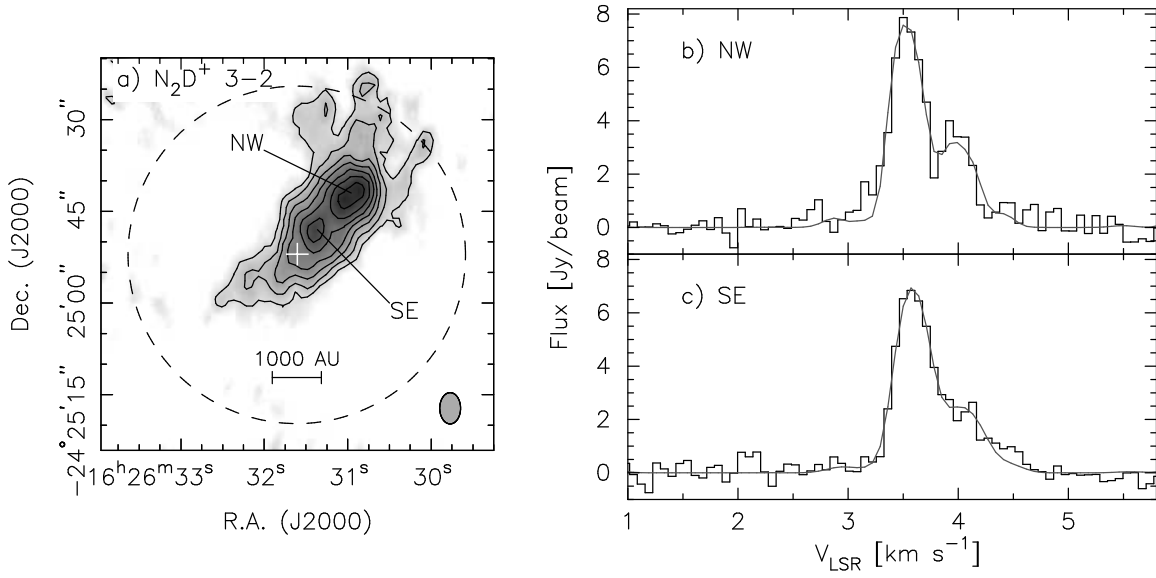


Fig. 8.— Spectra at the integrated line map peaks of N_2D^+ 3-2. (a) The integrated map as shown in Figure 1, with the locations of the two spectra indicated. The large dashed circle indicates the SMA primary beam size, while the small grey oval indicates the synthesised beam size. The white cross is the position of the peak integrated N_2H^+ 1-0 emission (DAM04). (b) The spectrum at position NW (histogram), with a model fit of the N_2D^+ 3-2 hyperfine structure (continuous line in grey). (c) The spectrum at position SE (histogram), with a model fit of the N_2D^+ 3-2 hyperfine structure (continuous line in grey).

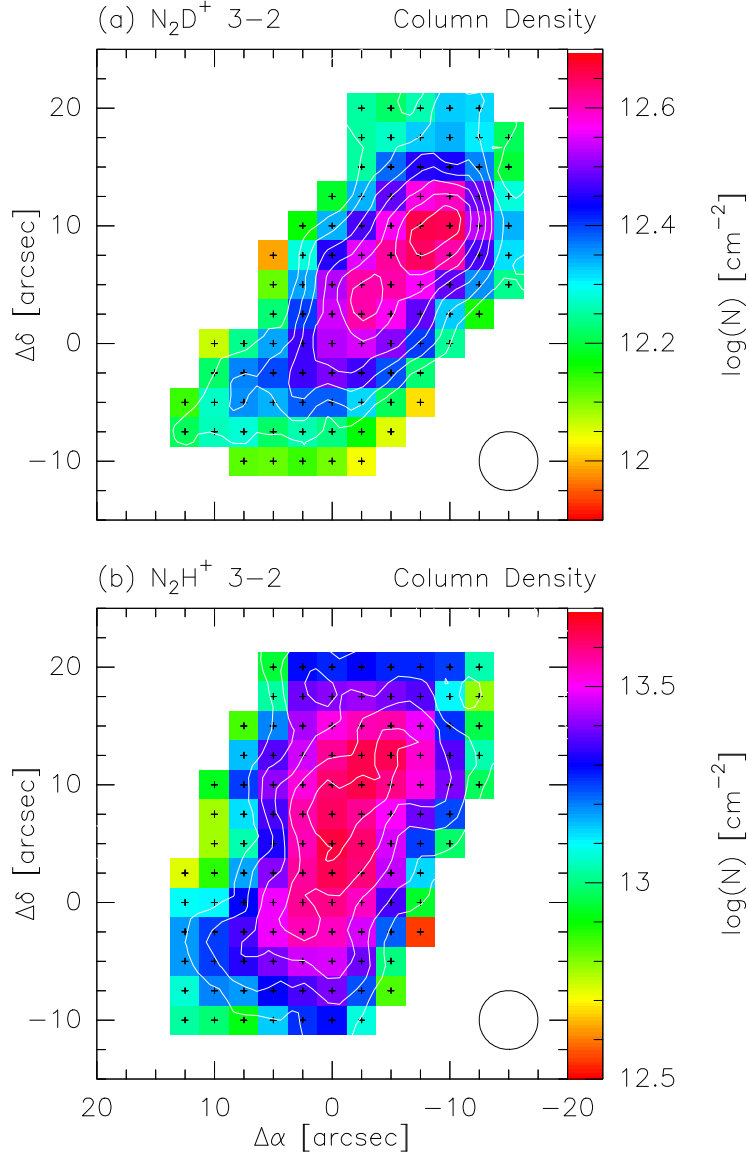


Fig. 9.— (a) Column density of N_2D^+ , assuming a constant excitation temperature of 10 K. The data have been resampled onto a $2''.5$ grid with a $5''$ circular beam (shown at lower right). The positions where the column density was determined are indicated by crosses. The contours represent the integrated intensity map of N_2D^+ and are the same as shown in Figure 1. (b) Column density of N_2H^+ , assuming a constant excitation temperature of 10 K. Other details are the same as in (a), except that the contours represent the integrated intensity map of N_2H^+ and are the same as shown in Figure 1. The origin of the maps is the position of the peak integrated N_2H^+ 1-0 emission (DAM04). [COLOUR FIGURE]

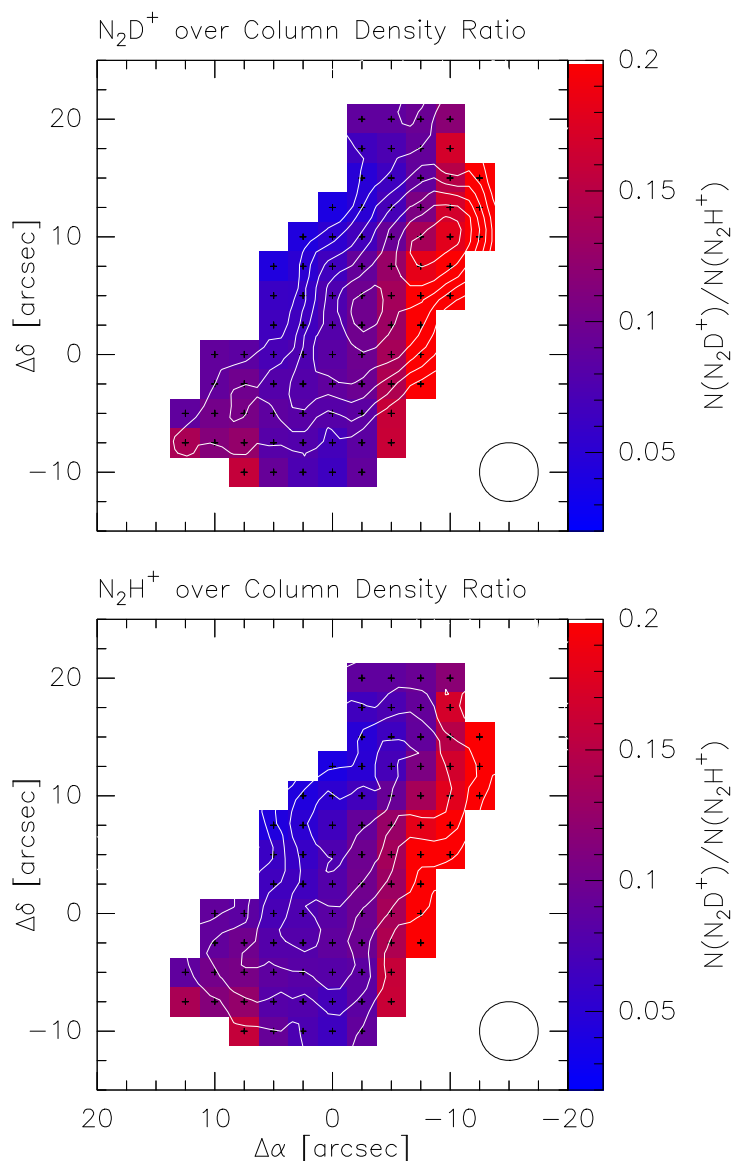


Fig. 10.— (a) Ratio of N₂D⁺ to N₂H⁺ column densities, using the results presented in Figure 9. The contours are integrated intensity of N₂D⁺ and are the same as shown in Figure 1. (b) Ratio of N₂D⁺ to N₂H⁺ column densities, using the results presented in Figure 9. The contours are integrated intensity of N₂H⁺ and are the same as shown in Figure 1. The resolution of the observations is indicated by the circular beam (shown at lower right). The origin of the maps is the position of the peak integrated N₂H⁺ 1-0 emission (DAM04). **[COLOUR FIGURE]**

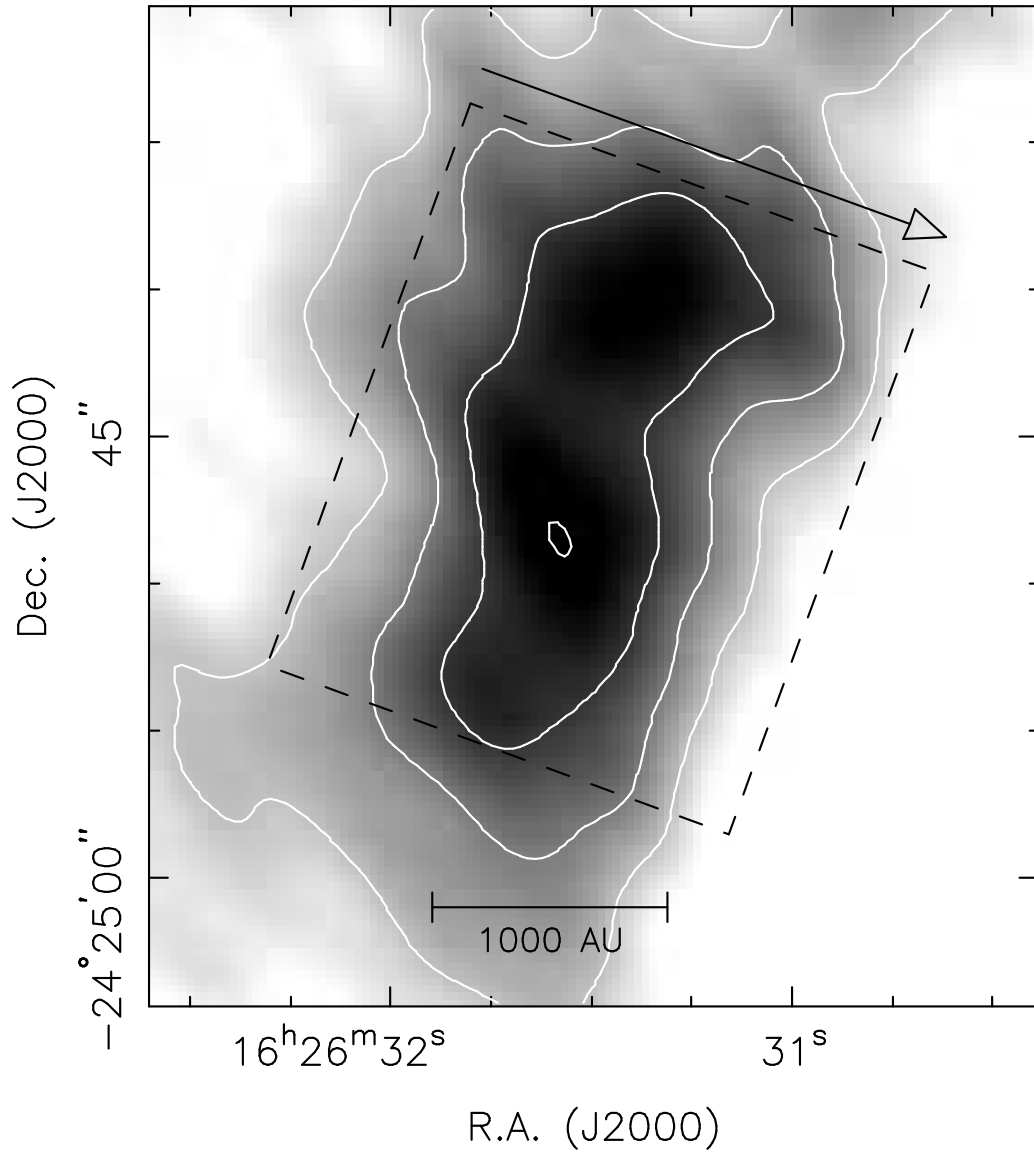


Fig. 11.— Location of the N₂H⁺ 3-2 radial column density cuts used to construct the radial profile shown in Figure 12. The box indicates the area from which the cuts were extracted, with the vector indicating the direction of the cuts. The image is the low resolution column density map, with contour levels of 1.5, 2.5, 3.6, and 4.6 × 10¹³ cm⁻².

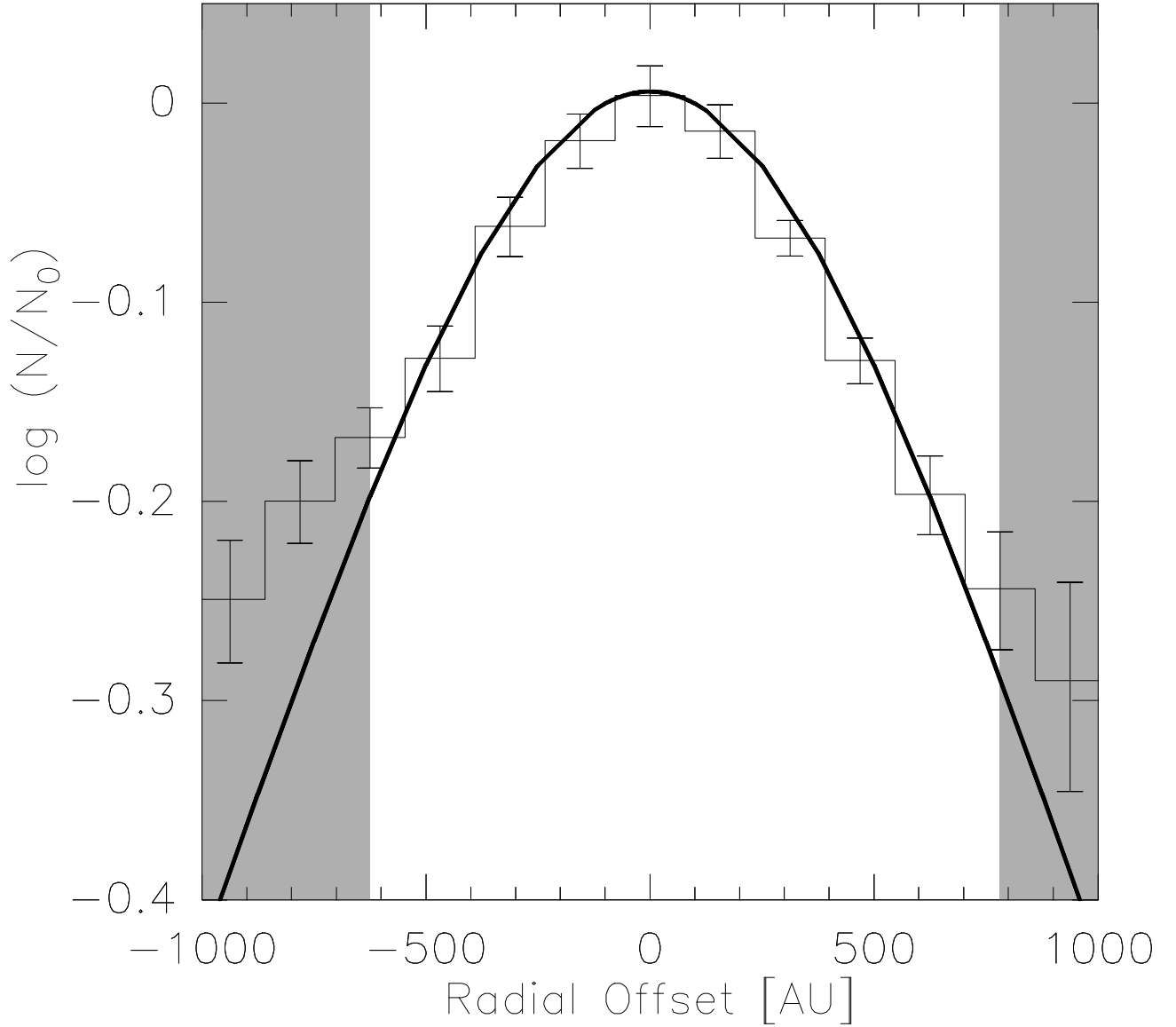


Fig. 12.— Normalized mean N_2H^+ 3-2 radial column density cut parallel to the minor axis of N6 (histogram), constructed from a series of cuts across N6 that were averaged and then normalized to the peak value. The dark continuous line represents a model of an isothermal cylinder whose parameters are described in §4.3. The model shown here has the values of radius (800 AU), kinetic temperature (20 K) and peak N_2H^+ column density ($4.6 \times 10^{13} \text{ cm}^{-2}$) fixed prior to comparison with the data, an N_2H^+ abundance (2.75×10^{-10}), determined by matching the model to the data (by eye), with a resultant peak density of $7.0 \times 10^6 \text{ cm}^{-3}$ and scale length of 365 AU. The shaded grey areas indicate where the data and model differ significantly and the core begins to merge into the background emission.